

Article

# Airborne Testing of 2- $\mu$ m Pulsed IPDA Lidar for Active Remote Sensing of Atmospheric Carbon Dioxide

Tamer F. Refaat <sup>1,\*</sup>, Mulugeta Petros <sup>1</sup>, Charles W. Antill <sup>1</sup>, Upendra N. Singh <sup>2</sup>, Yonghoon Choi <sup>3</sup>, James V. Plant <sup>4</sup>, Joshua P. Digangi <sup>5</sup> and Anna Noe <sup>1</sup>

<sup>1</sup> Remote Sensing Branch, NASA Langley Research Center, Hampton, VA 23681, USA; tamer.f.refaat@nasa.gov (T.F.R.); mulugeta.petros-1@nasa.gov (M.P.); charles.w.antill@nasa.gov (C.W.A.); anna.m.noe@nasa.gov (A.N.)

<sup>2</sup> NASA Engineering and Safety Center, NASA Langley Research Center, Hampton, VA 23681, USA; upendra.n.singh@nasa.gov

<sup>3</sup> Science Systems & Applications, Inc., Hampton, VA 23666, USA; yonghoon.choi-1@nasa.gov

<sup>4</sup> Material and Structures Experimental Research Branch, NASA Langley Research Center, Hampton, VA 23681, USA; james.v.plant@nasa.gov

<sup>5</sup> Atmospheric Chemistry and Dynamics Branch, NASA Langley Research Center, Hampton, VA 23681, USA; joshua.p.digangi@nasa.gov

\* Correspondence: tamer.f.refaat@nasa.gov

**Citation:** Refaat, T.F.; Petros, M.; Antill, C.W.; Singh, U.N.; Choi, Y.; Plant, J.V.; Digangi, J.P.; Noe, A. Airborne Testing of 2- $\mu$ m Pulsed IPDA Lidar for Active Remote Sensing of Atmospheric Carbon Dioxide. *Atmosphere* **2021**, *12*, 412. <https://doi.org/10.3390/atmos12030412>

Academic Editors: Dmitry Belikov

Received: 18 February 2021

Accepted: 18 March 2021

Published: 23 March 2021

**Publisher's Note:** MDPI stays neutral with regard to jurisdictional claims in published maps and institutional affiliations.



**Copyright:** © 2021 by the authors. Licensee MDPI, Basel, Switzerland. This article is an open access article distributed under the terms and conditions of the Creative Commons Attribution (CC BY) license (<http://creativecommons.org/licenses/by/4.0/>).

**Abstract:** The capability of an airborne 2- $\mu$ m integrated path differential absorption (IPDA) lidar for high-accuracy and high-precision active remote sensing of weighted-average column dry-air volume mixing ratio of atmospheric carbon dioxide ( $X_{CO_2}$ ) is demonstrated. A test flight was conducted over the costal oceanic region of the USA to assess instrument performance during severe weather. The IPDA targets  $CO_2$  R30 absorption line using high-energy 2- $\mu$ m laser transmitter. HgCdTe avalanche photodiode detection system is used in the receiver. Updated instrument model included range correction factor to account for platform attitude. Error budget for  $X_{CO_2}$  retrieval predicts lower random error for longer sensing column length. Systematic error is dominated by water vapor ( $H_2O$ ) through dry-air number density derivation, followed by  $H_2O$  interference and ranging related uncertainties. IPDA  $X_{CO_2}$  retrieval results in  $404.43 \pm 1.23$  ppm, as compared to  $405.49 \pm 0.01$  ppm from prediction models, using consistent reflectivity and steady elevation oceanic surface target. This translates to 0.26% and 0.30% relative accuracy and precision, respectively. During gradual spiral descend, IPDA results in  $404.89 \pm 1.19$  ppm as compared model of  $404.75 \pm 0.73$  ppm indicating 0.04% and 0.23% relative accuracy, respectively. Challenging cloud targets limited retrieval accuracy and precision to 2.56% and 4.78%, respectively, due to  $H_2O$  and ranging errors.

**Keywords:** carbon dioxide; active remote sensing; IPDA lidar; airborne testing

## 1. Introduction

Atmospheric carbon dioxide ( $CO_2$ ) is a dominant greenhouse gas that contributes to global warming and climate change, while influencing the carbon cycle on Earth. Understanding  $CO_2$  sources, sink and transport flux is critical for the scientific community and policy makers. Mitigating carbon dioxide upsurge is a social benefit that requires continuous monitoring and assessments through current techniques and improved technologies [1]. Atmospheric  $CO_2$  monitoring techniques rely on either in situ air sampling or remote sensing. In situ  $CO_2$  sampling is conducted using ground-based networks and airborne campaigns [2,3]. The former provides continuous sampling with limited spatial resolution, while the later offers higher spatial but limited temporal observations. Remote sensing of  $CO_2$  is conducted using passive and active techniques. Advanced space-based passive remote sensors, such as the Orbiting Carbon Observatory (OCO) missions, provide

wide spatial and temporal CO<sub>2</sub> monitoring. OCO-2 is a free-flyer that records spectral radiance variations of reflected sunlight from Earth's surface using high-resolution passive spectrometers [4]. OCO-3 is an upgraded instrument installed onboard the International Space Station for enhanced coverage of CO<sub>2</sub> measurements, while improving the accuracy and resolution [5]. Relying on sunlight introduces some spatial and temporal limitations such as absence of nighttime and seasonal high-latitude measurements. In addition, retrieval issues arise due to aerosol abundance, thin cloud conditions, and over complex terrains with rapidly changing surface reflectivity and elevations [6]. Active remote sensing of CO<sub>2</sub>, based on lidar techniques, is an alternative that potentially overcomes the limitations of passive sensors [6,7].

An active sensor provides its own radiation source that can be tuned to target specific absorption features of an atmospheric molecule using the differential absorption lidar (DIAL) technique. An airborne range-resolved (RR) DIAL could provide CO<sub>2</sub> vertical profile measurements independent of geographical location and time with straightforward retrieval algorithms. For further improving CO<sub>2</sub> measurement uncertainties, the integrated path differential absorption (IPDA) lidar is a special DIAL that provides a weighted average measurement of the gas over a sampling volume rather than RR profile. IPDA lidar relies on hard target returns providing high signal-to-noise ratio (SNR) resulting in high-precision and high-accuracy measurements [6–8]. Based on National Research Council recommendation, NASA initiated the Active Sensing of CO<sub>2</sub> Emissions over Nights, Days, and Seasons (ASCENDS) mission, which involves several groups for developing different CO<sub>2</sub> IPDA lidar instruments [7,9]. These instruments use either pulsed or continuous wave laser transmitters operating at 1.6- or 2.0- $\mu\text{m}$  wavelengths. Both wavelengths match optimum sensing absorption features for CO<sub>2</sub>, with additional ranging capability for pulsed techniques. ASCENDS objective was to achieve CO<sub>2</sub> measurement precision and accuracy of <0.3 ppm and <1.2 ppm, respectively, using a space-based lidar for 10-s average over Rail Road Valley [6,7]. NASA Langley Research Center (LaRC) has been involved in maturing high-energy pulsed lasers for CO<sub>2</sub> and wind lidar transmitters based on 2- $\mu\text{m}$  laser technology [10]. Combining both measurement capabilities potentially address CO<sub>2</sub> flux observations, recently advocated for by the Decadal Survey, to enhance studies of the gas transport phenomena [1].

Targeting the CO<sub>2</sub> R22 absorption line, RR-DIAL measurements were demonstrated as early as 2010, using a ground-based zenith pointing 2- $\mu\text{m}$  DIAL. DIAL transmitter used Ho:Tm:LuLiF technology producing 90-mJ pulses at 5-Hz repetition rate. Transmitted pulses were alternated between fixed off-line and on-line wavelengths set to either 2.15 or 2.80 GHz offset from line center. The receiver employed a direct detection system using an infrared (IR) phototransistor [11,12]. Column CO<sub>2</sub> measurements were attempted using the same instrument and the results were compared to NOAA tower in situ sampling at West Branch, Iowa (WBI) [13]. Adopting IPDA lidar technique, other instruments were developed at LaRC, after switching to the CO<sub>2</sub> R30 absorption line. R30 is compatible with Ho:Tm:YLF technology and offers some advantages including lower temperature sensitivity, lower molecular interferences and optimum optical depth for lower tropospheric CO<sub>2</sub> measurements. Implementing side-pumping configuration, a double-pulse 2- $\mu\text{m}$  IPDA lidar was developed with a 10 Hz pulse repetition rate. A single pump pulse was used to generate two successive laser pulses separated by 200  $\mu\text{s}$  with 90 and 45 mJ transmitted energies. The first pulse was tuned, within 1 to 6 GHz with respect to R30 line center, then locked to generate the on-line wavelength. The wavelength of the second pulse was locked to a fixed off-line position. Short time separation between transmitted pulses enhances ground footprint overlap for airborne applications [14]. The IPDA detection was based on commercial extended-range InGaAs pin detector. The instrument was tested on ground in horizontal configuration using 859 m away calibrated hard target with 19% reflectivity. Results indicated range measurement precision of 0.93 m and CO<sub>2</sub> weighted-average column dry-air volume mixing (XCO<sub>2</sub>) measurement precision of 2.24 ppm and accuracy of 0.44 ppm [15]. Airborne validation for the same instrument included

different conditions for ocean and land targets [16,17]. Retrievals of XCO<sub>2</sub> resulted in 4.15-ppm precision and 1.14-ppm accuracy achieved using 10-s average from a 6-km altitude over ocean [16]. Higher altitude resulted in enhanced range precision due to the domination of random detection noise on range error. Sensitivity analysis addressed atmospheric water vapor (H<sub>2</sub>O) potential effect on systematic errors for CO<sub>2</sub> measurements [6,18].

High variability of atmospheric H<sub>2</sub>O influences IPDA CO<sub>2</sub> measurement through direct molecular interference, spectral line broadening and dry-air number density derivation [6]. To address this issue, the same technology was upgraded to produce three successive pulses, for each pump pulse, for simultaneous measurements of CO<sub>2</sub> and H<sub>2</sub>O [18]. Upgrades included end-pumping for higher repetition rate (50 Hz) operation, while using fixed wavelengths for all pulses [19]. The selected wavelength positions were locked to 32-, 6.5- and 16-GHz offsets with respect to the R30 line for the first, second, and third pulses, respectively [18,20]. Although ground and airborne testing demonstrated the capability of the triple-pulse IPDA technique, using fixed 6.5-GHz on-line for CO<sub>2</sub> measurements resulted in a lower differential optical depth (about 0.1) while losing the tuning capability. With detection noise dominating random error, lower optical depth deteriorates measurement precision [21]. Focusing on CO<sub>2</sub> measurements, the IPDA was switched back to operate in double-pulse mode taking advantage of the high repetition rate in conjunction with tunable on-line transmitter. In addition, an advanced mercury cadmium telluride (HgCdTe or MCT) electron-initiated avalanche photodiode (e-APD) detection system was introduced to complement the InGaAs pin (PIN) detection channel [22]. The goal is to achieve high-precision and high-accuracy XCO<sub>2</sub> measurement with tunable CO<sub>2</sub> weighting function for adaptive targeting [6]. Assessment of XCO<sub>2</sub> retrieval random and systematic errors was presented using horizontal ground testing. Results indicated 1.11- and 0.33-ppm measurement accuracy and precision, equivalent to 0.26% and 0.08% systematic and random errors, respectively, obtained using 13.6% target reflectivity and operating at 0.5-GHz on-line offset. Range measurements indicate 0.7-m precision and 0.2-m accuracy [8].

Airborne testing campaign was conducted for the same instrument in late 2019. The campaign included four flights, consuming about 15-h airborne time, using the NASA B-200 aircraft. This paper presents the XCO<sub>2</sub> measurement results using the 2- $\mu$ m pulsed IPDA lidar during a local four-hour flight conducted on 17 September 2019. The flight objective was to capture land and ocean targets during day and night transition. The flight took-off and landed at Hampton, Virginia, during tropical storm Imelda. Flight plan started before sunset by heading southwest toward Wilmington, North Carolina, followed by south track over ocean until sunset, then heading back on the same route after sunset. Due to concurrent storm, weather conditions limited clear access to land targets. Therefore, cloud-top targets were attempted at higher airborne altitude for capturing free-tropospheric XCO<sub>2</sub>. The plan included two descending spirals, before and after sunset, over land during scarce clear-sky conditions. Moderate-state ocean surface was targeted, during clear sky conditions, off-shore Wilmington between the spirals.

## 2. Airborne 2- $\mu$ m Pulsed IPDA Lidar

A schematic for the 2- $\mu$ m pulsed IPDA lidar is shown in Figure 1. The instrument is designed for airborne operation, with nadir orientation, comprising a payload compatible with small research aircrafts. The total instrument size is 0.6 m<sup>3</sup>, and weights 430 kg, with steady-state power consumption of 2 kW [21]. The IPDA transmitter is set to produce two 2- $\mu$ m laser pulses for each pump pulse. Transmitter control and monitors units alternate the wavelength of each of the transmitted pulses between on- and off-line wavelengths using the seed laser, while monitoring transmitted pulse properties and providing time synchronization among different units. Laser pulses are transmitted co-axially through the telescope secondary. The collected return radiation is directed toward the aft-optics integrated to the side of the telescope. Aft-optics collimates, splits then focuses the return radiation into the two signal channels. A free-space PIN and fiber-coupled MCT e-APD

detection systems were used for the high- and low-signal channels, respectively [22]. A data acquisition system digitizes and stores the collected data for real-time signal processing and inspection. Full instrument description is given in [8] and Table 1 lists the main instrument parameters and relevant settings during airborne operation.

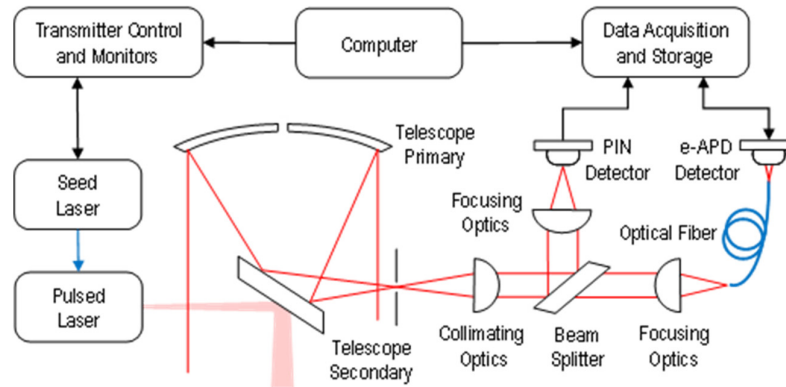


**Figure 1.** A schematic for the 2- $\mu\text{m}$  pulsed IPDA lidar for atmospheric  $\text{CO}_2$  measurements. The transmitter is based on 2- $\mu\text{m}$  double-pulse high-energy laser, seed laser and transmitter control and monitors unit for setting the wavelength of each transmitted pulse and time synchronization. The receiver telescope focuses return radiation onto two detection channels based on InGaAs PIN and MCT e-APD detectors. Data acquisition and storage unit records and stores the IPDA data. A computer is used for instrument operation control, monitoring, and real-time data processing.

**Table 1.** Parameters and relevant settings for the 2- $\mu\text{m}$  IPDA Lidar during airborne double-pulse operation for atmospheric  $\text{CO}_2$  measurements.

<b>Transmitter</b>	
Off-Line Wavelength	2051.1905 nm (15.93 GHz)
On-Line Wavelength (Tunable)	2050.875–2051.010 nm (0.5–3.0 GHz)
Pulse Energy (On/Off)	17.5/6 mJ
Beam Divergence	180 $\mu\text{rad}$
Beam Diameter	16 mm
Electrical-to-optical Efficiency	1.0%
<b>Receiver</b>	
Telescope Diameter	0.4 m
Field-of-View	350 $\mu\text{rad}$
Optical Efficiency	65%
<b>Low-Signal (10%) Channel using PIN Detection System</b>	
Detector Type	InGaAs pin photodiode
Detector Responsivity	1.15 A/W
Detector Diameter	300 $\mu\text{m}$
TIA Gain, Bandwidth, NEP	$10^4$ V/A, 10 MHz, 55 pW/Hz <sup>1/2</sup>
<b>High-Signal (90%) Channel using e-APD Detection System</b>	
Detector Type	HgCdTe e-APD
Detector Responsivity	1.05 A/W
Detector Size	80 $\times$ 80 $\mu\text{m}^2$ pixel (4 $\times$ 4 pixels)
Avalanche and TIA Total Gain	$1.1 \times 10^8$ V/W at 12 V and 77 K
Bandwidth, NEP	6 MHz, 9.2 fW/Hz <sup>1/2</sup>

### 2.1. IPDA Lidar Transmitter

The IPDA lidar transmitter is a 2- $\mu\text{m}$  high-energy pulsed laser based on double-end pumping of two Ho:Tm:YLF crystals. A 792-nm AlGaAs laser diode source is used to provide 800 mJ pump energy at 50 Hz repetition rate [19]. Relative to the pump pulse, Q-switch trigger generates successive 2- $\mu\text{m}$  laser pulses with time separation that can be adjusted between 150 and 500  $\mu\text{s}$ . For a fixed total output energy, up to 80 mJ, time adjustment controls the pulse-width and energy distribution between the transmitted pulses. Depending on the IPDA measurement objective, the number of transmitted pulses and wavelength of each pulse are selected, synchronized and switched using the transmitter control unit. Each pulse is injection seeded with a pre-selected wavelength using the ramp-and-fire technique [20]. Custom semiconductor-distributed feedback laser diodes are used as seed source by implementing standard Pound–Drever–Hall frequency stabilization scheme in reference to the R30 line and a gas cell [8,23]. In double-pulse operation mode, a tunable on-line and a fixed off-line wavelengths, are set for the first and second pulses, respectively. Tunable on-line wavelength selection targets the R30 side-line, while off-line is fixed at 2051.1905 nm (15.93 GHz), as shown in Figure 2. The figure compares line positions to CO<sub>2</sub> spectra calculated for sea-level and 5 km altitude using HITRAN data base and Voigt line model [18,24,25]. Spectral profile variation between these two levels is due to atmospheric temperature and pressure change with altitude [6,18].

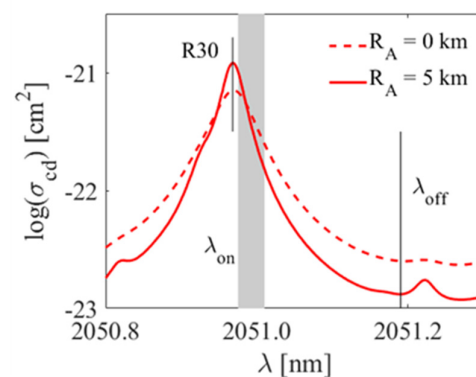


**Figure 2.** Transmitted on- and off-line wavelength settings for the 2- $\mu\text{m}$  IPDA lidar, in double pulse operational mode, with respect to CO<sub>2</sub> absorption spectra around R30 line. The spectra are calculated for sea-level and 5 km altitudes using HITRAN 2016 [18,24]. Gray area and black line mark the tunable on-line range and the fixed off-line wavelength positions.

Continuous monitoring for the energy and wavelength of the transmitted laser pulses is conducted during the IPDA operation. Energy and wavelength monitors were developed and calibrated to provide real-time, per-shot, measurement for these parameters. These measurements are critical for the IPDA technique, allowing energy normalization between pulses and wavelength drift and jitter corrections [8]. Energy normalization and wavelength corrections significantly reduce transmitter-related systematic errors, or biases, in CO<sub>2</sub> measurements providing better accuracy. A high-speed, extended-range InGaAs pin detector is integrated to monitor pulse energies. Calibration of the detector output converts an optical sample of the transmitted pulse power into energy [15]. This process results in high SNR, over 900 and 400 for on- and off-line, respectively, due to accessible of high-signals close to the source. Careful dynamic range setting is required to maintain linearity and avoid additional XCO<sub>2</sub> systematic errors [26]. A heterodyne photo-receiver is integrated within the laser enclosure for monitoring the wavelength properties of the transmitted laser pulses. This photo-receiver is based on high-bandwidth, fiber-coupled, dual-balanced, extended-range, InGaAs photodiodes and a trans-impedance

amplifier (TIA). The photodiodes mix a small optical sample of the output laser pulse with a 100-MHz frequency-shifted optical sample of the seed laser. The photo-receiver produces a heterodyne signature that is processed in real-time using fast Fourier transform to confirm seeding success, and quantify minuscule wavelength shifts of the transmitted laser pulse relative to the seeding wavelength. This defines the transmitted wavelength drift and jitter, per-pulse and per-shot [8].

Figure 3 demonstrates the stability of the IPDA lidar 2- $\mu\text{m}$  laser transmitter through more than 3 h continuous operation during 17 September 2019 flight. Figure 3a indicates a transmitted on-line energy measurement of  $17.5 \pm 0.2$  mJ. The figure also shows transmitted off-line energy enhancement from  $4.0 \pm 0.2$  mJ to  $6.1 \pm 0.3$  mJ, through fine tuning the pump energy. During airborne operation, higher absorption loss through longer propagation range is experienced by the on-line wavelength. This is compensated by transmitting a higher on-line energy compared to off-line. Figure 3b shows the wavelength variation of the transmitted on- and off-line pulses, with respect to the seeding wavelength. Continuous real-time observation of this data confirms the success of the seeding process, while quantifying wavelength drift and jitters. The presented results show on- and off-line shifts of  $0.04 \pm 0.02$  and  $0.05 \pm 0.07$  pm, respectively, as measured with respect to their wavelength offsets. For example, on-line wavelength drift of 0.021 pm/hr is observed for 3 GHz offset, which could add 0.1% to the XCO<sub>2</sub> systematic error at sea-level if not accounted for.

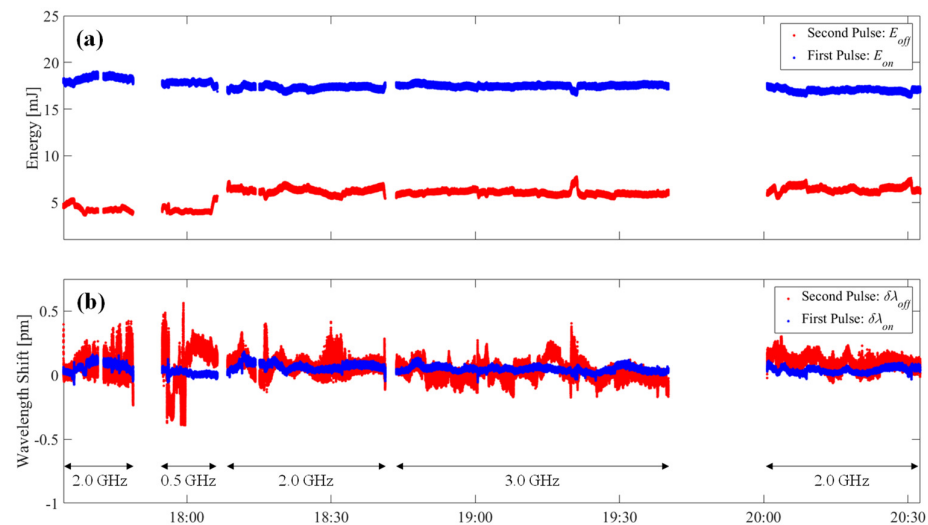


**Figure 3.** Continuous real-time monitoring for the 2- $\mu\text{m}$  IPDA laser transmitter operation during 17 September 2019 flight. (a) Laser pulse energy variation records using the laser energy monitor. (b) Wavelength variation records, with respect to seeding wavelength setting, using heterodyne seeding monitor. Monitoring is conducted per shot, for on-line and off-line, set for the first and second pulses, respectively. Different on-line tuning, of 0.5, 2.0 and 3.0 GHz with respect to R30 line center, were used during airborne operations.

## 2.2. IPDA Lidar Receiver and Data Acquisition

The IPDA receiver consists of a Newtonian telescope formed by primary and secondary mirrors, as shown in Figure 1. The primary is a 0.4-m diameter aluminum hyperbolic, which focuses the return radiation to a 300- $\mu\text{m}$  diameter spot size. The secondary is a flat fused silica with high reflective dielectric coating, on both surfaces, for 2- $\mu\text{m}$  at 45°. This mirror directs the return radiation in to aft-optics, while transmitting the expanded laser beam coaxially with the telescope. Field-imaging aft-optics is used, which consists of an aperture, collimating and focusing optics and a beam-splitter. The aft-optics splits the radiation to 90% and 10% high- and low-signal detection channels, while reducing the focus spot size to 85- $\mu\text{m}$  diameter at the detector plane. Direct detection was implemented for

both signal channels to reduce speckle effect [27,28]. The high-signal channel consists of the PIN detection system including custom designed, dc-coupled, 10 MHz TIA. The diameter of the detector sensitive area is 300- $\mu\text{m}$ , which was selected larger than the focus size, to reduce beam steering jitter effects on the collected radiation during airborne operations. PIN detection channel exhibits a background noise of 2-mV measured as the standard deviation of the detector output while blocking the transmitted beam. This translates to a noise-equivalent-power (NEP) of 55 pW/Hz<sup>1/2</sup> [8].

The MCT e-APD detection system was used for the low-signal channel. Recently, a similar e-APD detection system was validated for 1.6- $\mu\text{m}$  IPDA lidar applications at NASA Goddard Space Flight Center (GSFC) [29,30]. The e-APD consists of 16 pixels, arranged in 4  $\times$  4 pixel-array, with 80  $\times$  80  $\mu\text{m}^2$  pixel-size. The device is integrated with readout electronics that accesses each pixel through individual, variable gain TIA. Electronics produce the summation of selected number of pixels through operational software. The software sets the bias voltage and the TIA gains as well as monitor the device temperature. The detection system includes a vacuum setup for cooling the device, to 77 K, using a cryo-cooler to reduce dark current and noise. Additional optics couples and focus the input radiation onto the center 2  $\times$  2 pixels. Limiting the number of active pixels reduces the total noise budget of the detection system. The whole system was integrated in a rack mountable chassis at GSFC [30]. Detection system characterization at LaRC resulted in 63.35% quantum efficiency, equivalent to 1.05 A/W current responsivity, at 77 K and 2- $\mu\text{m}$  radiation. Increasing the bias voltage increases the device gain up to 587.5 obtained at 12 V. At this bias, the total NEP of the detection system is 5.9 fW/Hz<sup>1/2</sup> for the selected 4 center pixels at highest TIA gain setting. NEP increase to 9.2 fW/Hz<sup>1/2</sup> at the lowest TIA gain setting used for this study [31]. The high-gain and limited detection bandwidth result in NEP limited performance.

The IPDA signals are digitized and stored using the data acquisition unit, which is based on two similar high-performance 12-bit, two-channel digitizers. The digitizers continuously sample the inputs at a fixed rate of 1 GS/s. Laser Q-switch signal triggers a data storage event that includes a selected pre- and post-trigger samples. Pre-trigger samples are used for background correction. One digitizer is dedicated for transmitted energy and wavelength monitors, with a fixed record length. The other digitizer is used for the IPDA returns from the high- and low-signal channels, with a variable record length set by post-trigger samples depending on airborne altitude. For each detection channel, the full-scale input of the digitizer (1 V) defines the maximum detectable power, whereas the minimum detectable power is equal to the total NEP (in W) of the detection channel. Figure 4 shows the dynamic range of the IPDA combined detection systems spanning the minimum and maximum detectable powers for both channels. Although lowest TIA gain of the e-APD channel was used for this study, the highest gain reduces the minimum detectable power limit. PIN detection channel complement the e-APD by extending the maximum detectable power range. For example, the IPDA detectable power span over 6 order of magnitudes (58 dB), which is achievable at e-APD bias voltages of 10 V. Lower bias voltages results in overlap between low and high-signal channels, while higher bias results in undetectable gap (around 10<sup>-7</sup> W). Additionally, the figure marks, in vertical lines, the return power ranges for different airborne measurement conditions, as compared to ground testing [8]. Due to higher return power during ground testing, IPDA operation focused on the PIN detection channel. This study focuses on results obtained using low-signal e-APD detection channel set at the lowest TIA gain.

### 2.3. IPDA Lidar Support Instruments

Meteorological and geographical data (MGD) are required during IPDA airborne operation for modeling instrument performance and converting the differential optical depth measurements into XCO<sub>2</sub>. These data are obtained from support instruments operating independently but in conjunction with the IPDA onboard the aircraft. Support instruments include Global Positioning System (GPS), Inertial Navigation System (INS), and

meteorological and in situ sensors. GPS records IPDA lidar platform time, used for instruments synchronization, and geolocation in terms of altitude, latitude and longitude. The INS records platform attitude, in the form of roll, pitch and yaw navigation angles. A meteorological sensor records ambient temperature and pressure at platform altitude. A commercial cavity ring-down spectrometer (G2301-m, PICARRO) was used for in situ measurement of dry-air mixing ratios of H<sub>2</sub>O and CO<sub>2</sub>. Ambient air was sampled using a TAT probe modified for particle-rejecting air sampling. For CO<sub>2</sub>, a three-point calibration was performed before and after flight using NOAA traceable standard. H<sub>2</sub>O was calibrated through laboratory inter-comparison with a NIST-traceable chilled mirror hygrometer. As a result, in situ precision and accuracy for CO<sub>2</sub> were 0.1 ppm and 0.5 ppm, respectively, while H<sub>2</sub>O total uncertainty was 0.05%, or 500 ppm.

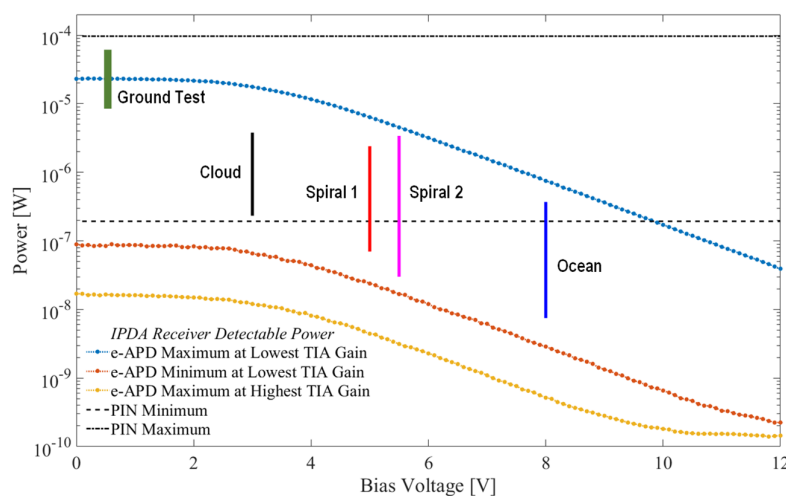
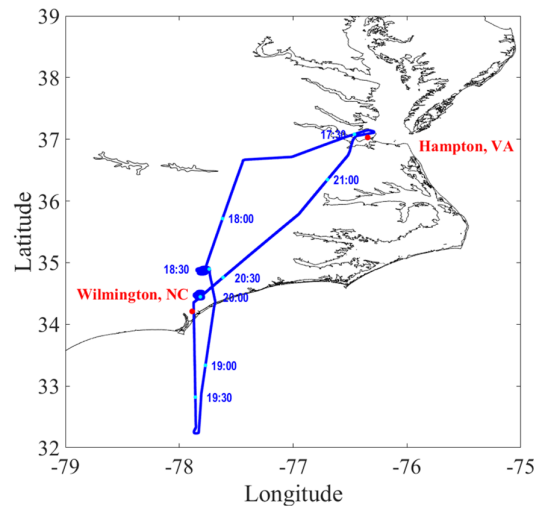


**Figure 4.** Dynamic range of the IPDA return power based on combining the high- and low-signal channels power limits, using PIN and e-APD detection systems, respectively. Dynamic range is defined by minimum and maximum detectable powers for steady operating conditions. At a fixed operating temperature of 77 K, dynamic range of the e-APD varies with the device voltage bias. Minimum power limit can be enhanced by setting TIA at higher gain. PIN is independent on bias voltage and included for comparison with e-APD. Vertical line mark return power range during September 17, 2019 flight for clouds (black), spirals 1 and 2 (red and purple) and ocean (blue) testing, as compared to ground testing (green) reported in [8].

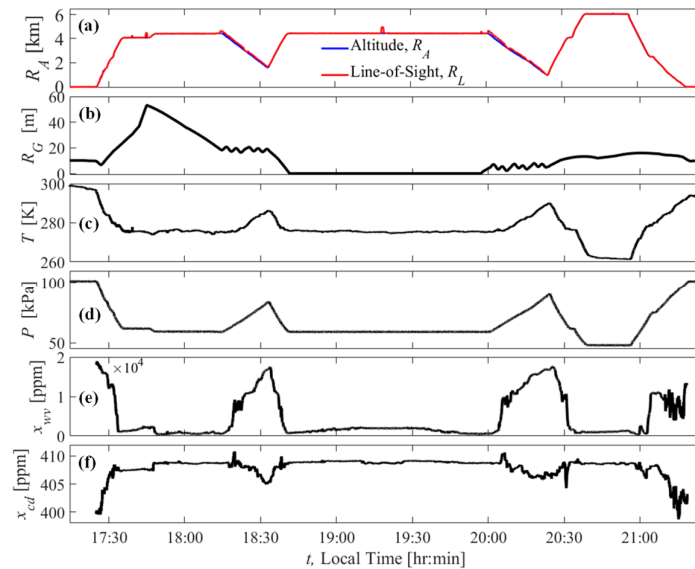
Figure 5 shows the NASA B-200 ground track for the IPDA lidar testing flight conducted on 17 September 2019. The flight took-off, at 5:25 pm, local time, from Hampton and headed southwest, over land, toward Wilmington. Cloudy weather conditions limited IPDA LOS to cloud tops (Cloud record), preventing full atmospheric penetration to ground surface. Taking advantage of short clear-sky condition over land, a spiral descent was conducted (Spiral 1 record), before flying over the ocean offshore Wilmington. Targeting ocean in moderate surface state and clear-sky weather, the flight continues south until sunset (Ocean 1 record), when it headed back north (Ocean 2 record) toward Wilmington. Then, a second spiral descent was conducted (Spiral 2 record) again over land in clear-sky condition, before heading back and land at Hampton, at 9:20 pm.

Figure 6 shows the corresponding MGD records, obtained from the support instruments, presented versus local time. Local time was obtained using GPS universal time coordinate (UTC) conversion. Roll and pitch angles are used to convert the airborne altitude to line-of-sight (LOS) distance used to validate the IPDA column length measurements. Flight altitude,  $R_A$ , and LOS,  $R_L$ , records are obtained using 10 S/s sampling rate, as shown in Figure 6a. Latitude and longitude are used to define target surface as well as deriving ground elevation,  $R_G$ , using a 1° resolution global digital elevation model (DEM),

as shown in Figure 6b. Temperature,  $T$ , and pressure,  $P$ , are obtained using the meteorological sensor, as shown in Figure 6c,d. Figure 6e,f show  $H_2O$  and  $CO_2$  dry-air mixing ratios,  $x_{wv}$  and  $x_{cd}$ , respectively, obtained using the in situ sensor. Metrological and in situ sensors operate at 1 S/s sampling rate. Linear interpolation is used to convert different MGD sampling time to IPDA acquisition time for single-shot analysis. The V-shape profiles of Figure 6a mark the spiral descends. Spiral 1 record started before sunset at 6:15 pm from 4.4 km, descending to lowest altitude of 1.6 km at 6:33 pm, with a descend rate of 2.6 m/s., followed by ascending back to 4.4 km with rate of 6.1 m/s at 6:41 pm. Spiral 2 record started after sunset at 8:00 pm from 4.4 km, descending to lowest altitude of 935.9 m at 8:24 pm, with a descend rate of 2.4 m/s. Then, ascend back to 4.1 km with rate of 6.6 m/s at 20:32 pm.



**Figure 5.** Flight ground track (blue) recorded using GPS for NASA B-200 aircraft on 17 September 2019 between Hampton, VA (37.0299° N, 76.3452° W) and Wilmington, NC (34.2104° N, 77.8868° W) for 2- $\mu$ m IPDA lidar airborne testing. Sunsets was at 7:16 PM local time at Wilmington on that date.



**Figure 6.** MGD records obtained using IPDA lidar support instruments during airborne operation onboard NASA B-200 aircraft on 17 September 2019. The records include (a) GPS and INS altitude measurement and line-of-sight calculations, (b) DEM ground elevation, (c) temperature and (d) pressure from the meteorological sensor, and (e) water vapor and (f) carbon dioxide dry-air mixing

ratios from the PICARRO in situ sampler. All records are presented versus local time, derived using GPS UTC time.

The calculated LOS, presented in Figure 6a, corresponds to the distance traveled by the transmitted laser from the IPDA to a ground target, equivalent to the IPDA sensing column length,  $R_C$ , as described in Figure 7. According to the figure,  $R_L$  can be predicted through flight altitude,  $R_A$ , and target elevation,  $R_G$ , with respect to sea-level, according to

$$R_L = (R_A - R_G) \cdot C_L, \quad (1)$$

where  $C_L$  is a range correction factor arise due IPDA airborne attitude, by which  $R_L$  will deviate from a perfect nadir pointing system along the aircraft ground projection line, as shown in Figure 7. Solving for the angle between LOS and its ground projection,  $\theta$ ,

$$\theta = \tan^{-1} \left[ \sqrt{\tan^2(\theta_R) + \tan^2(\theta_P)} \right], \quad (2)$$

where  $\theta_R$  and  $\theta_P$ , are roll and pitch angles, respectively. Thus,  $C_L$  is given by

$$C_L = 1/\cos(\theta). \quad (3)$$

In this analysis yaw angle is not included, since yaw rotation is about the IPDA optical axis parallel to aircraft yaw axis, providing geometric symmetry with respect to LOS. The value of  $C_L$  is close to unity, during normal operation and slightly higher than unity during sharp aircraft maneuvers such as spirals.

Figure 7 indicates that DEM driven ground elevation,  $R'_G$ , could be different than the true ground elevation at the laser footprint,  $R_G$ . The difference tends to zero for IPDA operating over calm-state ocean and nonzero over land. Although the difference can be estimated for different land target topographies using high-resolution DEM, it is undetermined for cloud tops and rough-state ocean. Given that meteorological models are defined vertically along aircraft ground projection,  $C_L$  must be included in differential optical depth derivation and  $XCO_2$  retrievals to account for the true LOS column measurements. Otherwise IPDA retrievals could suffer significant bias due to incorrect ranging.

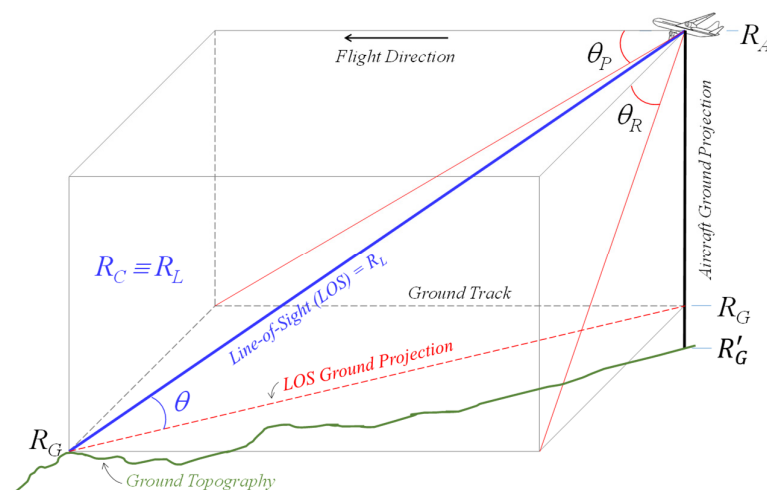


**Figure 7.** A schematic for IPDA sensing column length,  $R_C$ , equivalent to line-of-sight,  $R_L$  (blue line), calculated using airborne altitude,  $R_A$ , ground elevation,  $R_G$ , and the range correction factor estimated from aircraft roll and pitch angles,  $\theta_R$  and  $\theta_P$ , respectively.  $R_C$  is measured using the pulsed IPDA lidar itself, using time-of-flight technique. Range correction factor is applied for transforming MGD and standard atmospheric models from aircraft ground projection line to LOS.

### 3. CO<sub>2</sub> IPDA Lidar Modeling

For IPDA double-pulse operating mode, CO<sub>2</sub> double-path differential optical depth,  $\Delta\tau_{cd}$ , is the main product, with ranging as a byproduct.  $\Delta\tau_{cd}$  can be obtained from the total measured double-path differential optical depth,  $\Delta\tau$ , after correcting for other interfering atmospheric molecules. In the vicinity of R30, H<sub>2</sub>O is the dominant interfering molecule, and therefore

$$\Delta\tau_{cd}(\lambda_{off}, \lambda_{on}, R_A, R_G) = \Delta\tau(\lambda_{off}, \lambda_{on}, R_A, R_G) - \Delta\tau_{wv}(\lambda_{off}, \lambda_{on}, R_A, R_G) \quad (4)$$

where  $\Delta\tau_{wv}$  is the H<sub>2</sub>O double-path differential optical depth. Equation (4) is defined for a nadir pointing airborne IPDA operating at on- and off-line wavelengths  $\lambda_{on}$  and  $\lambda_{off}$ , respectively, and an altitude  $R_A$  pointing to a target at an elevation  $R_G$ . The measured  $\Delta\tau$  is obtained by the natural logarithm of the ratio of the received off- and on-line return energy (integrated power), after normalization to respective transmitted energies, according to

$$\Delta\tau(\lambda_{off}, \lambda_{on}, R_A, R_G) = \ln \left\{ \frac{P(\lambda_{off}, R_A, R_G) \cdot t(\lambda_{off})/E(\lambda_{off})}{P(\lambda_{on}, R_A, R_G) \cdot t(\lambda_{on})/E(\lambda_{on})} \right\} \quad (5)$$

where  $P$  is the measured return power,  $t$  is the return laser pulse-width, and  $E$  is the transmitted energy for on- and off-line wavelengths seeding pulses 1 and 2, respectively (i.e.,  $\lambda_{on} = \lambda_1$ ,  $\lambda_{off} = \lambda_2$ ,  $E(\lambda_{on}) = E_1$  and  $E(\lambda_{off}) = E_2$  of Figure 3). Return power is calculated using the equation

$$P = I/(T \cdot G_A \cdot \mathfrak{R}) \quad (6)$$

For both on- and off-line signals, where  $I$  is the integration of the return signal and  $G_A$  and  $\mathfrak{R}$  are the e-APD gain and voltage responsivity based on the bias voltage setting. For the same conditions,  $\Delta\tau_{cd}$  can be modeled using the Equation

$$\Delta\tau_{cd}(\lambda_{off}, \lambda_{on}, R_A, R_G) = 2 \cdot \int_{R_A}^{R_G} \Delta\sigma_{cd}(\lambda_{off}, \lambda_{on}, r) \cdot N_{cd}(r) \cdot dr \quad (7)$$

where  $\Delta\sigma_{cd}$  is the CO<sub>2</sub> differential absorption coefficient, obtained at the sensing wavelengths and the corresponding temperature and pressure at range,  $r$ , and  $N_{cd}$  is the CO<sub>2</sub> number density. The integration is performed with respect to the range along the aircraft ground projection line, as shown in Figure 7. Equation (7) is also applicable for H<sub>2</sub>O. For IPDA model derivation and XCO<sub>2</sub> retrieval, time dependent MGD presented in Figure 6c–f are converted to altitude profiles, as shown in Figure 8. This was conducted by averaging the data within a 200-m range bin, followed by linear interpolation to enhance the resolution to 1-m. This results in a regional scale trends for  $T$ ,  $P$  and  $x_{wv}$  that follows Mid-Latitude Summer (MLS) atmospheric model [32]. Lower near-surface  $x_{cd}$  is observed due to vegetation intake during daytime followed by higher constant trend toward higher altitude, which is compared to a constant profile at 408 ppm.

Applying both MGD and MLS model profiles of Figure 8 to Equation (7),  $\Delta\tau_{cd}$  and  $\Delta\tau_{wv}$  are calculated versus range as shown in Figure 9. In this figure, range variation was depicted as altitude variation for fixed target elevation at sea-level (blue curves), as well as variation of target elevation for a fixed airborne altitude of 6.5 km (green curves). Higher target elevation accounts for high altitude cloud targets. The model was repeated using 1, 2, and 3 GHz on-line offsets from R30 line. The figure presents the theoretical performance of an ideal 2- $\mu$ m IPDA measuring  $\Delta\tau_{cd}$  aiming perfect nadir. CO<sub>2</sub> results indicated an insignificant difference between  $\Delta\tau_{cd}$  calculated using MGD profiles and MLS model. This is due to minor pressure differences and R30 insensitivity to temperature. Lower  $\Delta\tau_{wv}$ , as compared to  $\Delta\tau_{cd}$ , predicts low molecular interference for XCO<sub>2</sub> measurement. However, deviations in  $\Delta\tau_{wv}$  modeling using MGD and MLS are attributed to large deviations in  $x_{wv}$  profiles as shown in Figure 8, which could result in significant biases if not corrected for. To include the effect of the airborne platform attitude, considering  $\Delta\tau_{cd}$  measurement along the true LOS shown in Figure 7, Equation (7) is updated to

$$\Delta\tau_{cd}(\lambda_{off}, \lambda_{on}, R_A, R_G) = 2 \cdot C_L \cdot \int_{R_A}^{R_G} \Delta\sigma_{cd}(\lambda_{off}, \lambda_{on}, r) \cdot N_{cd}(r) \cdot dr \quad (8)$$

for actual modeling during airborne measurements. In addition,  $R_L$ , from Equation (1), can be compared to the IPDA measured column length,  $R_C$ , which is obtained using time-of-flight technique. In this technique time delay between the transmitted and received laser pulses,  $\Delta t$ , is converted into column length or range according to

$$R_C = c \cdot \Delta t / 2 \quad (9)$$

where  $c$  is the speed of light. Equating Equations (1) and (9) result in deriving target elevation at the laser footprint from IPDA measurement and GPS altitude.

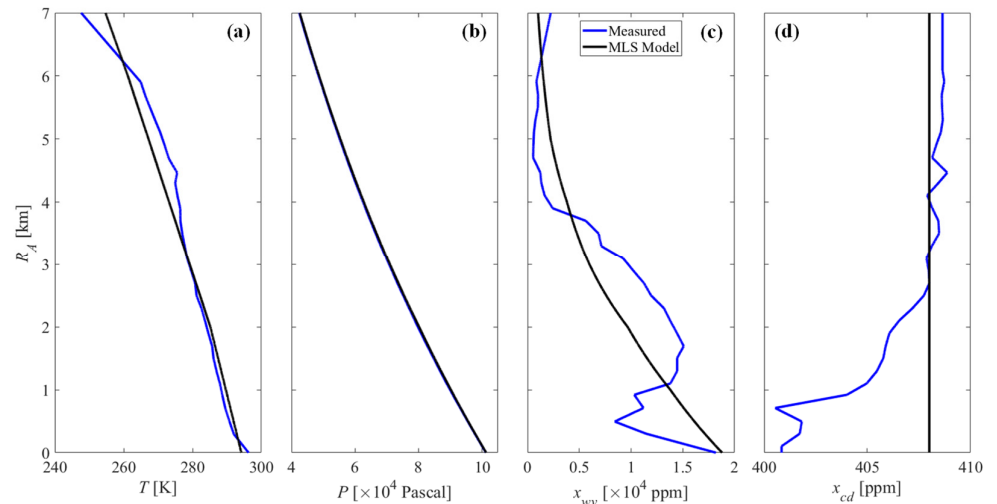


**Figure 8.** Vertical profiles of (a) temperature, (b) pressure, and dry-air mixing ratios of (c) water vapor and (d) carbon dioxide during IPDA lidar airborne testing onboard NASA B-200 aircraft conducted on 17 September 2019. Processing included 200-m range-bin averaging and 1-m linear interpolation for the data presented in Figure 6. The profiles are compared to MLS atmospheric model, except for carbon dioxide, which is assumed constant at 408 ppm.

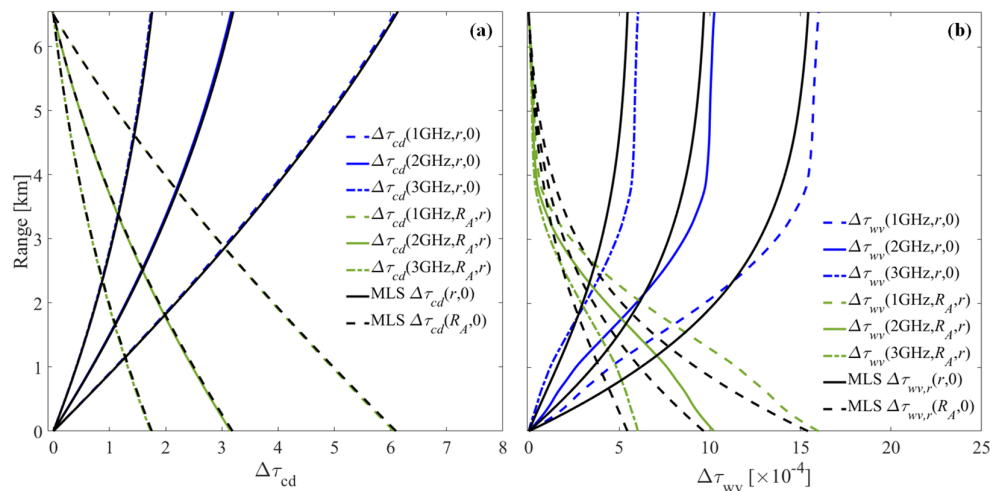


**Figure 9.** Modeling of the 2- $\mu$ m IPDA lidar double-path differential optical depth for (a) measured CO<sub>2</sub>,  $\Delta\tau_{cd}$ , and (b) interfering H<sub>2</sub>O,  $\Delta\tau_{wv}$  assuming perfect nadir operation. Results obtained using MGD (colored curves) and MLS model (black curves), presented in Figure 8 using on-line wavelengths of 1, 2 and 3 GHz. Range represents variable flight altitude for constant sea-level elevation (blue curves) and variable ground elevation for a constant flight altitude of 6.5 km (green curves).

### 3.1. XCO<sub>2</sub> Retrieval

The 2-μm IPDA lidar measured  $\Delta\tau_{cd}$ , from Equation (5), can be converted into XCO<sub>2</sub> using MGD through the integration of the weighting function [8,16]. By definition, CO<sub>2</sub> dry-air volume mixing ratio,  $x_{cd}$ , is given by

$$x_{cd}(r) = 10^6 \cdot N_{cd}(r)/N_{dry}(r) \tag{10}$$

where  $N_{dry}$  is the dry-air number density, obtained by subtracting H<sub>2</sub>O number density,  $N_{wv}$ , from total air number density calculated using the Ideal Gas law, according to

$$N_{dry}(r) = P(r)/k \cdot T(r) - N_{wv}(r) \tag{11}$$

where  $k$  is the Boltzmann's constant. For fixed off-line wavelength, substituting Equation (10) into (8) results in

$$\Delta\tau_{cd}(\lambda_{on}, R_A, R_G) = 2 \times 10^{-6} \cdot C_L \cdot \int_{R_A}^{R_G} \Delta\sigma_{cd}(\lambda_{on}, r) \cdot N_{dry}(r) \cdot x_{cd}(r) \cdot dr. \tag{12}$$

A well-mixed atmospheric gases, such as CO<sub>2</sub>, exhibit almost constant vertical profile, as shown for  $x_{cd}$  in Figure 8. In this case Equation (12) can be re-written as

$$X_{cd}(\lambda_{on}, R_A, R_G) = \Delta\tau_{cd}(\lambda_{on}, R_A, R_G)/2 \times 10^{-6} \cdot C_L \cdot W_{cd}(\lambda_{on}, R_A, R_G) \tag{13}$$

where  $X_{cd}$  represents XCO<sub>2</sub> and  $W_{cd}$  is the CO<sub>2</sub> integrated weighting function defined as

$$W_{cd}(\lambda_{on}, R_A, R_G) = \int_{R_A}^{R_G} \Delta\sigma_{cd}(\lambda_{on}, r) \cdot N_{dry}(r) \cdot dr \tag{14}$$

Equation (13) is used for  $X_{cd}$  retrieval, converting the IPDA measured  $\Delta\tau_{cd}$  into XCO<sub>2</sub>. The Equation indicates the dependence of  $X_{cd}$  on the on-line wavelength and the sensing column length, represented by Equation (9), which relies on both airborne altitude and ground elevation.

To examine  $X_{cd}$  retrieval from the IPDA lidar measurement,  $\Delta\tau_{cd}$  model results, of Figure 9a, were applied to Equation (13) and presented in Figure 10. Model  $X_{cd}$  is derived using MGD, of Figure 8, with respect to variations in both altitude and target elevation.

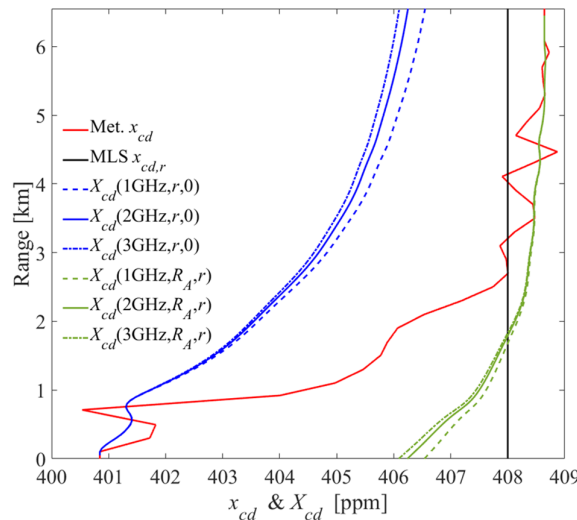


**Figure 10.** MGD and MLS CO<sub>2</sub> dry-air volume mixing ratio  $x_{cd}$  profiles compared to modeling of  $X_{cd}$  retrieval from the 2-μm IPDA lidar modeled measurements assuming perfect nadir operation. Range represents variable flight altitude for constant sea-level elevation (blue curves). Range represents variable ground elevation for a constant flight altitude of 6.5 km (green curves). Results obtained using MGD and modeled  $\Delta\tau_{cd}$ , of Figures 8 and 9, respectively, for on-line wavelengths of 1, 2 and 3 GHz. The figure indicates small difference between  $x_{cd}$  and  $X_{cd}$ , independent of on-line wavelength, for shorter column length.

Comparing  $x_{cd}$  in situ measurement and modeled  $X_{cd}$  profiles indicates a difference that is inherent to the IPDA technique due to the weighted average technique. Ideally, this difference is equal to zero if and only if  $x_{cd}$  profile is constant with respect to altitude, implying a perfect well-mixing condition as assumed in the MLS model. Otherwise, a difference will exist between  $x_{cd}$  and  $X_{cd}$  depending on measurement altitude and target elevation. Assuming sea-level target elevation, higher airborne altitude results in higher difference between  $x_{cd}$  and  $X_{cd}$  with pronounced  $\lambda_{on}$  dependence. On the contrary, assuming 6.5 km airborne altitude, lower target elevation results in higher difference and stronger  $\lambda_{on}$  dependence. Generally, shorter sensing column length results in closer  $x_{cd}$  and  $X_{cd}$  independent of  $\lambda_{on}$ .

### 3.2. XCO<sub>2</sub> Retrieval Errors

Errors in  $X_{cd}$  retrievals result from uncertainties in both IPDA  $\Delta\tau_{cd}$  measurement and MGD sampling limitations. These uncertainties are divided into random and systematic errors, affecting  $X_{cd}$  precision and accuracy, respectively. Random error is dominated by detection noises associated with IPDA return signals, which exhibit normal distribution that can be reduced by shot averaging. According to Equation (5), absolute random error of  $X_{cd}$ ,  $\delta X_{cd}$  in ppm, can be expressed as [8,18,33]

$$\delta X_{cd}(\lambda_{on}, R_A, R_G) = \frac{1}{\sqrt{N}} \cdot \frac{\sqrt{SNR_{p,on}^{-2} + SNR_{p,off}^{-2}}}{2 \times 10^{-6} \cdot C_L \cdot W_{cd}(\lambda_{on}, R_A, R_G)} \quad (15)$$

where  $N$  is the number of shot average, and  $SNR_{p,on}$  and  $SNR_{p,off}$  are the SNR of the on- and off-line return power, respectively. In this Equation, SNR of laser energy monitor is considered high enough [8] and speckle SNR is enhanced by shot averaging and receiver aperture [27,28]. Equation (15) can estimate the IPDA  $X_{cd}$  retrieval random error at any operating condition. For example, according to Figure 4, assuming 10 V bias of the e-APD detection channel, and the return on- and off-line powers are set to span the full dynamic range (by adjusting the respective transmitted energies), then a maximum SNR will be achieved for both signals. Under these optimum conditions Figure 11a shows  $\delta X_{cd}$  variation with altitude for sea-level target elevation and different on-line wavelengths. Results indicate that operating at higher altitude, equivalent to a longer sensing column length, reduces  $\delta X_{cd}$  for any on-line wavelength setting. For a fixed altitude, lower  $\delta X_{cd}$  is achieved for on-line closer to R30 line center.

Systematic errors of  $X_{cd}$ ,  $\Delta X_{cd}$  in ppm, are generated from different independent sources that include sensitivities to MGD and ranging. In this analysis, transmitter related systematic errors are disregarded due to heterodyne monitoring, which is used for correcting wavelength drift and jitter. For example, systematic error due to temperature was estimated by calculating  $X_{cd}$  sensitivity to atmospheric temperature deviation of  $\Delta T = \pm 10$  K according to

$$\Delta X_{cd}(\Delta T) = \max(|\Delta X_{cd}(T) - \Delta X_{cd}(T \pm \Delta T)|). \quad (16)$$

The selected  $\Delta T$  corresponds to the maximum standard deviation of the bin-averaging for profile derivation of Figure 8. Equation (16) is applicable to all other error sources, which were evaluated numerically. Figure 11b shows the variation of  $X_{cd}$  systematic error with altitude, presented for deviations of  $\Delta P = \pm 750$  Pascal,  $\Delta x_{wv} = \pm 1000$  ppm and  $\Delta R_c = \pm 10$  m for atmospheric pressure, water vapor and column length, respectively. Although higher variations could occur, the figure indicates that systematic errors due to temperature and pressure are negligible due to R30 line properties and consistency of atmospheric pressure. H<sub>2</sub>O influence  $X_{cd}$  retrieval mainly through dry-air number density derivation, which is almost independent on the IPDA operating state. If this error is suppressed, through regular updated profiling, using spirals or drop sondes for example, interference and ranging become dominant. Figure 11b also indicates that operating the IPDA with on-line closer to the R30 center reduces the influence of all error source except ranging.

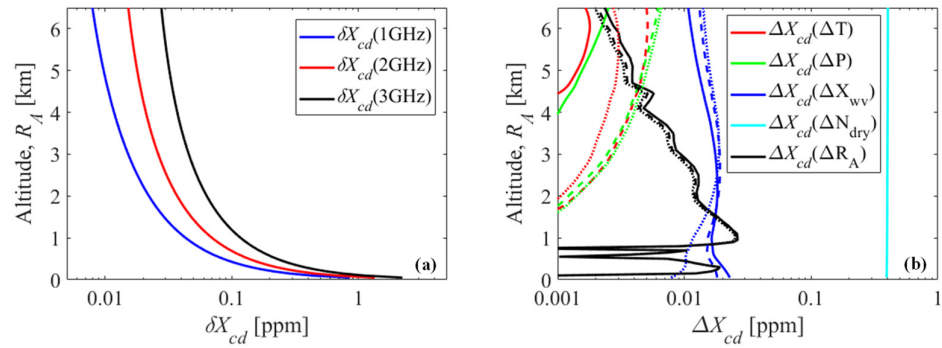


**Figure 11.** Estimated XCO<sub>2</sub> (a) random error,  $\delta X_{cd}$ , and (b) systematic error,  $\Delta X_{cd}$ , variation with altitude for the 2- $\mu\text{m}$  IPDA lidar.  $\delta X_{cd}$  is modeled using MCT e-APD detection channel set at 10 V bias and assuming full dynamic range return signals for achieving maximum SNR and 500 shot (10-s) average.  $\Delta X_{cd}$  is modeled assuming  $\Delta T = \pm 10$  K,  $\Delta P = \pm 750$  Pascal,  $\Delta X_{wv} = \pm 1000$  ppm and  $\Delta R_c = \pm 10$  m for atmospheric and ranging error sources using 1 GHz (solid), 2 GHz (dashed) and 3 GHz (dotted) on-line wavelengths.

#### 4. IPDA Lidar Measurements

Figure 12 shows airborne profiles for the IPDA lidar acquired on and off-line energy monitor and return signals using the e-APD channel. On-line transmitted energy is set to a higher value than the off-line, as shown in Figure 12a. Figure 12b shows the on- and off-line return signals with four distinct features. High residual scattering, occurs around 1.5  $\mu\text{s}$  with respect to pre-trigger, due to aircraft window, which coincide with the energy monitor signals. This is followed by high scattering off near-field high-altitude Cirrus clouds at 5  $\mu\text{s}$ , then a lower magnitude scattering off lower-altitude Cumulus clouds at 19  $\mu\text{s}$ , and finally far-field ground at 31  $\mu\text{s}$ . The figure lists the range and altitude for the atmospheric features, and Figure 12c–e focus on their profiles. In Figure 12c on-line starts with higher magnitude, compared to off-line, due to the higher transmitted energy setting, while Figure 12d shows both signals at almost equal magnitude due to on-line absorption loss. For ground return, shown in Figure 12e, longer sensing column length leads to even stronger on-line absorption due to higher CO<sub>2</sub> content. Ground return represents a hard target characterized by uniform Gaussian profile that resembles the laser pulse shape represented by the energy monitor. Whereas cloud return contains finer details due to target density variation within the laser spot as indicated in Figure 12c,d. This captures the IPDA lidar capability using the state-of-the-art 2- $\mu\text{m}$  transmitter and advanced e-APD detection for sensing atmospheric CO<sub>2</sub>. Accumulating similar profiles, Figure 13 shows a color diagram for the airborne 2- $\mu\text{m}$  successive range-corrected backscatter. The off-line return was used to construct the plot during cloudy conditions providing consistent return power due to weaker absorption. Return signals are collected using the e-APD channel, set at 3 V, with color representing the logarithm of the range-corrected signal strength. Signal processing included time synchronization, background subtraction, energy normalization and 1-s (50) shot average. The figure reveals mostly dense high-altitude clouds cover over land due to the coinciding tropical storm, with some limited ground access during clear conditions. Flight altitude was maintained at 4.4 km during that record.

Data processing for IPDA XCO<sub>2</sub> retrieval starts by integrating the pulses to obtain the return power, then  $\Delta\tau_{cd}$  calculation using single-shot data applied to Equation (5), followed by H<sub>2</sub>O correction and averaging. MGD is used to calculate  $W_{cd}$  using Equation (14), followed by XCO<sub>2</sub> retrieval using Equation (13). Other parameters are observed during this process including SNR, transmitted pulse width, energy and wavelength shifts. The model of Equation (8) is updated using MGD data to predict IPDA  $\Delta\tau_{cd}$  measurement and XCO<sub>2</sub> retrieval. Finally, a validation process is conducted based on comparing the IPDA XCO<sub>2</sub> retrievals from  $\Delta\tau_{cd}$  measurements,  $X_{cd,rr}$  to the modeled XCO<sub>2</sub> derived using MGD

at the same location,  $X_{cd,m}$ . Modeled  $X_{CO_2}$  is treated as an estimate value to assess the precision and accuracy for the IPDA retrieval. Relative IPDA retrieval precision,  $\epsilon_R$ , can be statistically estimated according to

$$\epsilon_R = \delta X_{cd} / X_{cd,r} = \sqrt{\delta X_{cd,r}^2 - \delta X_{cd,m}^2} / X_{cd,r} \tag{17}$$

which corresponds to the total relative random error, where  $\delta$  denote standard deviations of the proceeding variable. Relative IPDA retrieval accuracy,  $\epsilon_s$ , is estimated from

$$\epsilon_s = \Delta X_{cd} / X_{cd,r} = (X_{cd,r} - X_{cd,m}) / X_{cd,r} \tag{18}$$

corresponding to the total relative systematic error. During 17 September 2019 flight, five distinctive records, covering different environmental operating conditions for the IPDA lidar are discussed. Clear-sky ocean target before and after sunset (Ocean 1 and Ocean 2 during day and night, respectively), clear-sky spiral descend over land before and after sunset (Spiral 1 and Spiral 2 during day and night, respectively), and thick-cloud cover to capture free-tropospheric  $X_{CO_2}$ . A summary of the measurement settings and statistical results are presented in Table 2.

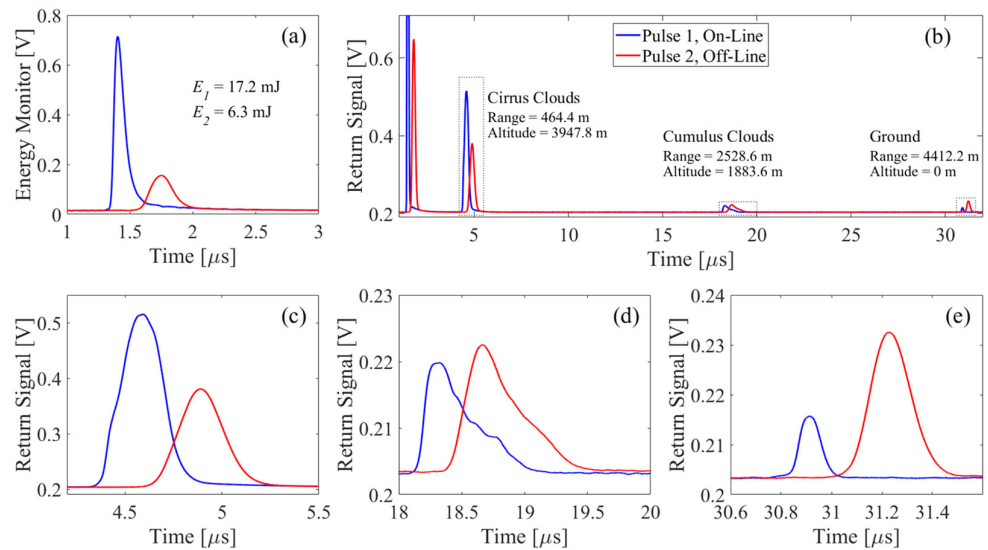


**Figure 12.** Sample of the 2- $\mu$ m IPDA lidar signal profiles collected during airborne operation on 17 September 2019 at 6:8:27 local time. (a) IPDA lidar transmitted energy monitor signals and (b) corresponding return signals obtained using e-APD detection channel, applied for  $CO_2$  remote sensing. Return profiles capture three distinctive features, as shown in the zoom-in for (c) Cirrus clouds, (d) Cumulus clouds and (e) ground. These represent the IPDA raw data processed by 10-sec (500) shot average obtained using 2-GHz on-line setting and 3 V e-APD bias voltage.

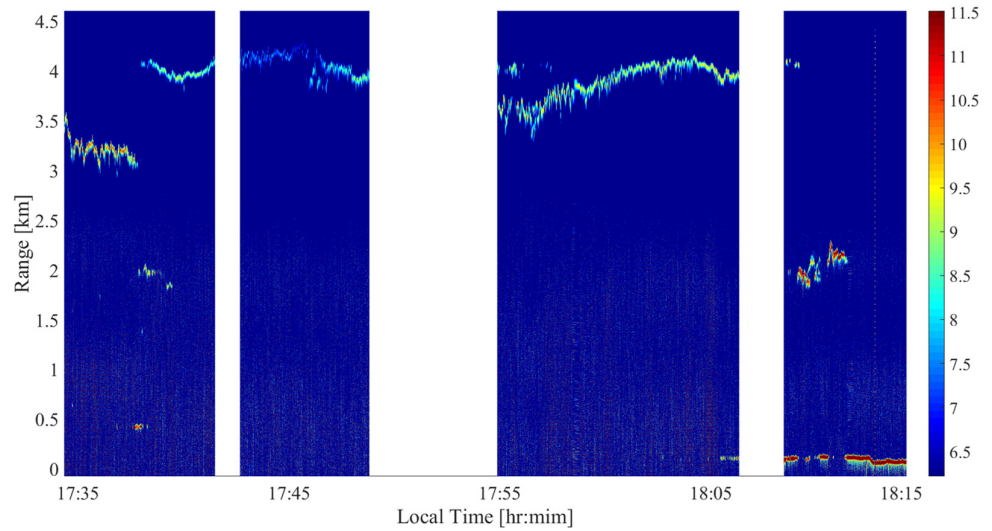


**Figure 13.** Airborne pulsed 2 mm IPDA lidar color diagram for range corrected off-line signals, using the e-APD detection channel set at 3 V bias voltage. Color legend represents signal strength in logarithmic scale. Signal processing included pulse synchronization, back ground subtraction, energy normalization and 1-s (50 shots) average. Vertical axis represent the range, spanning sea-level to flight altitude of 4.4 km, with 0.15 m resolution. Thick cloud cover prevents measurements from ground targets, except for some broken cloud events.

**Table 2.** Summary for the 2- $\mu\text{m}$  CO<sub>2</sub> IPDA lidar settings and measurement statistics for different airborne records conducted on 17 September 2019.

	Ocean 1	Ocean 2	Spiral 1	Spiral 2	Cloud
Total Shots	106,450	63,000	78,450	94,700	32,200
$\lambda_{\text{em}}$ (GHz)	3.0	3.0	2.0	2.0	0.5
$V_B$ (V)	8.0	8.0	5.0	5.5	3.0
$E_{\text{on}}$ (mJ)	$17.49 \pm 0.11$	$17.49 \pm 0.14$	$17.30 \pm 0.17$	$16.99 \pm 0.18$	$17.77 \pm 0.14$
$E_{\text{off}}$ (mJ)	$6.01 \pm 0.13$	$5.83 \pm 0.26$	$6.11 \pm 0.30$	$6.37 \pm 0.28$	$4.13 \pm 0.42$
$P_{\text{on}}$ ( $\mu\text{W}$ )	$0.14 \pm 0.05$	$0.22 \pm 0.05$	$0.50 \pm 0.20$	$0.50 \pm 0.30$	$1.90 \pm 0.80$
$P_{\text{off}}$ ( $\mu\text{W}$ )	$0.19 \pm 0.06$	$0.29 \pm 0.06$	$0.90 \pm 0.50$	$1.00 \pm 0.50$	$9.40 \pm 0.30$
$R_A$ (m)	4474.3	4474.8	4464.2 1610.7	4458.1 1240.1	4446.6
$R_C \pm \delta R_C$ (m)	$4474.8 \pm 2.0$	$4474.2 \pm 3.4$	$4644.3 \pm 9.5$ $1653.3 \pm 5.3$	$4684.3 \pm 20$ $1292.3 \pm 18$	$620.9 \pm 167.4$
$X_{\text{cd},m} \pm \delta X_{\text{cd},m}$ (ppm)	$405.49 \pm 0.01$	$405.49 \pm 0.02$	$404.75 \pm 0.73$	$404.58 \pm 0.90$	$408.26 \pm 0.20$
$X_{\text{cd},r} \pm \delta X_{\text{cd},r}$ (ppm)	$404.43 \pm 1.23$	$403.76 \pm 1.58$	$404.89 \pm 1.19$	$404.71 \pm 1.91$	$418.97 \pm 20.0$
$\Delta X_{\text{cd}}$ (ppm)	1.07	1.73	0.15	0.13	10.71
$\delta X_{\text{cd}}$ (ppm)	1.23	1.58	0.94	1.68	20.02
$\epsilon_S$ (%)	0.26	0.43	0.04	0.03	2.56
$\epsilon_R$ (%)	0.30	0.39	0.23	0.42	4.78

#### 4.1. Ocean Records

During airborne operations, the IPDA targeted ocean surface before and after sunset as shown in Figure 5. Oceanic surface is characterized by low but consistent surface reflectivity at 2- $\mu\text{m}$  and consistent sea-level target elevation. These are suitable conditions for validating the IPDA lidar for CO<sub>2</sub> sensing, while minimizing range and target reflectivity uncertainties. Long and fixed altitude flight over ocean provides stable operation and consistent measurement. Figure 14 shows the statistical analysis for single-shot  $\Delta\tau_{\text{cd}}$  records during ocean return obtained using 3 GHz and 8 V e-APD bias. The distribution of  $\Delta\tau_{\text{cd}}$ , shown in Figure 14a, was obtained by constructing a histogram, counting the number of occurrence of  $\Delta\tau_{\text{cd}}$  within 0.001 bins. The histogram fits to a normal distribution indicating

the domination of detection shot noise and enhance precision could be achieved through shot averaging. Allan-variance analysis, applied to  $\Delta\tau_{cd}$  as shown in Figure 14b, confirms shot-noise domination and estimates the limits of shot averaging. For example, Ocean 1 data record indicates that up to 1900 shot average (38-s) can be applied, which would result in  $3.4 \times 10^{-6}$  variance or 0.0019 standard deviation. This standard deviation is equivalent to 0.14% random error or precision, for a mean  $\Delta\tau_{cd}$  of 1.375 obtained for that record. Although a high shot average could be utilized, a moderate 500 shot (10-s) average was applied, as shown in Figure 15. The figure presents the airborne IPDA lidar measurements compared to updated models for ocean target. Data discontinuation, between 19:15 and 19:20, is due to sharp aircraft turn, as shown in Figure 5. Figure 15a compares IPDA column length measurement to LOS. IPDA  $\Delta\tau_{cd}$  measurement is compared to model in Figure 15b and  $X_{cd}$  retrieval compared to in situ and model in Figure 15c. Measurement data points within  $\pm 1$  standard deviation of the normal distribution fitting were selected for this analysis. This results in 47.4% and 62.0% success rate for Ocean 1 and Ocean 2 records, respectively. The success rate is defined as the ratio of the selected shots used in the final analysis to the total number of transmitted shots, as presented in Table 2. Results indicate consistent  $X_{cd}$  statistics between both records before and after sunset, with night time results tends to higher uncertainties. These higher uncertainties are caused by higher CO<sub>2</sub> variability due to land breeze, as confirmed by spiral records.

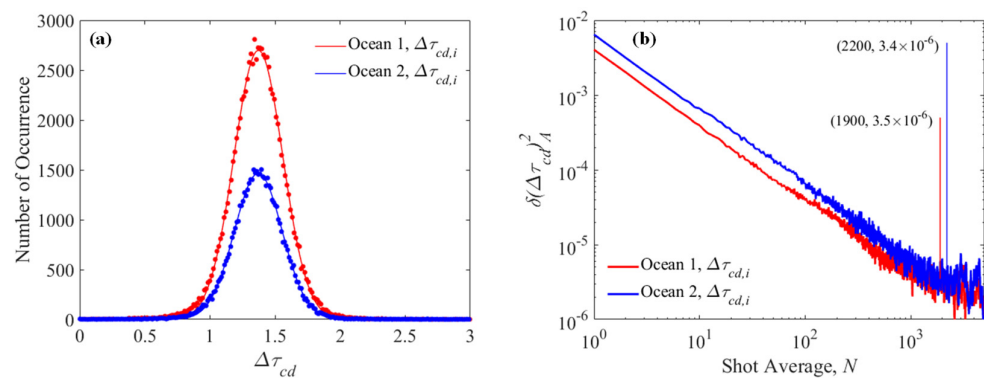


**Figure 14.** Statistical analysis for the 2- $\mu$ m IPDA lidar single-shot  $\Delta\tau_{cd}$  measurement. (a) Statistical distribution of  $\Delta\tau_{cd}$  data (dots) and normal distribution fitting (curves) indicating dominant shot noise. (b) Allan-variance analysis for single-shot  $\Delta\tau_{cd}$  confirming shot noise domination, which can be reduced by shot average exceeding the applied 10-s (500 shots).

#### 4.2. Spiral Records

Gradual airborne descend, in spiral format, provides an opportunity for updating local MGD variation with altitude during IPDA measurement for better  $\Delta\tau_{cd}$  modeling and XCO<sub>2</sub> retrieval. Besides, IPDA measurement variation with altitude provides an opportunity to perform additional range-bin averaging to enhance XCO<sub>2</sub> retrieval precision. The outcome is an  $X_{cd}$  altitude profile within spiral highest and lowest altitudes. Figure 16a shows the airborne altitude variation with time, as compared to LOS and IPDA column measurements. Ground elevation, presented in Figure 16b, was obtained by equating Equations (1) and (9) including the variation of  $C_L$ , shown in Figure 16c. During spiral maneuvers,  $C_L$  becomes critical to account for extending the IPDA column length due to aircraft banking, as indicated in Figure 7. The calculated ground elevation mean and standard deviation are  $10.88 \pm 6.78$  m, compared to DEM estimates of  $11.09 \pm 4.89$  m. The corresponding  $\Delta\tau_{cd}$  model was updated, within the spiral time, and shown in Figure 16d, as compared to the processed IPDA  $\Delta\tau_{cd}$  measurement. The final processed  $\Delta\tau_{cd}$  is applied for  $X_{cd}$  retrieval, using Equation (9), and compared to model and in situ measurements, as shown in Figure 16e.

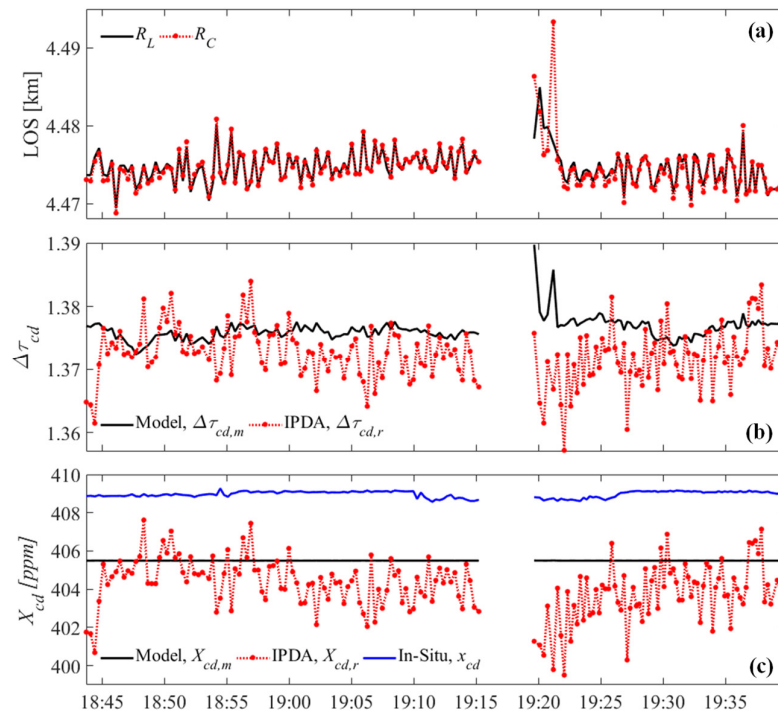


**Figure 15.** Airborne pulsed 2- $\mu\text{m}$  IPDA lidar measurement and retrieval results during Ocean 1 and Ocean 2 records obtained before and after sunset. (a) Airborne LOS,  $R_L$  as compared to IPDA column measurement,  $R_C$ . (b) IPDA  $\Delta\tau_{cd}$  measurement using 10-s (500 shots) average compared to model  $\Delta\tau_{cd}$  obtained from MGD. (c) IPDA retrieved  $X_{CO_2}$ ,  $X_{cd,r}$ , compared to model driven  $X_{CO_2}$ ,  $X_{cd,m}$  and corresponding  $x_{cd}$  in situ measurements. Measurements obtained using 3 GHz and 8 V e-APD bias.

A summary of IPDA  $\Delta\tau_{cd}$  processing and statistical analysis is presented in Figure 17 during spiral maneuver. Single-shot  $CO_2$   $\Delta\tau_{cd}$  measurement,  $\Delta\tau_{cd,i}$ , is obtained according to Equation (5) and shown in Figure 17a. Variation of  $\Delta\tau_{cd,i}$  with time captures strong column length dependence, with statistical histogram, shown in Figure 17b. The histogram diverts from normal distribution, indicating domination of other fluctuations than detection shot noise. In this case, excessive shot average could introduce processing related bias as confirmed by Allan-variance analysis, shown in Figure 17c. The analysis indicates a minimum variance of  $1.7 \times 10^{-4}$  obtained at only at 160 shot average. Both average and variance limits are caused by uncorrected range dependence. To correct for range dependence,  $\Delta\tau_{cd}$  was normalized to the IPDA column measurement, according to per-shot,  $i$ , as shown in Figure 17d. Repeating the histogram for  $\Delta\tau_{cd,R}$  results in better normal distribution fit indicating shot noise domination, as shown in Figure 17b, with enhanced Allan variance to  $6.7 \times 10^{-5}$  obtained at permissible higher shot average of 600, as shown in Figure 17c. This implies that higher shot average could be conducted without biasing the results. Further processing included selecting data points within  $\pm 1.5$  standard deviation of the normal distribution, as marked by black dots in Figure 16a,d, followed by 10-s (500 shots) average.

$$\Delta\tau_{cd,R} = \Delta\tau_{cd,i}/R_{C,i} \quad (19)$$

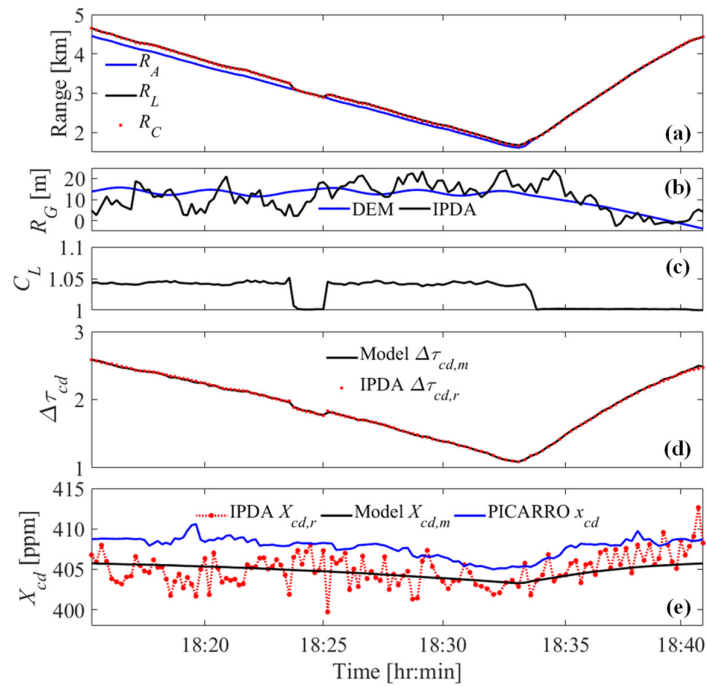


**Figure 16.** Airborne pulsed 2- $\mu\text{m}$  IPDA lidar measurement and retrieval results during Spiral 1 conducted before sunset. (a) Airborne altitude,  $R_A$ , as compared to LOS,  $R_L$  and IPDA column measurement,  $R_C$ . (b) Estimated ground elevation,  $R_G$ , as compared to DEM results. (c) Corresponding  $C_L$  profile used for converting  $R_A$  to  $R_L$ . (d) IPDA  $\Delta\tau_{cd}$  measurement after processing and 10-s (500 shots) average,  $\Delta\tau_{cd,r}$  compared to model  $\Delta\tau_{cd}$ ,  $\Delta\tau_{cd,m}$  obtained from MGD. (e) IPDA retrieved  $X_{CO_2}$ ,  $X_{cd,r}$  compared to model driven  $X_{CO_2}$ ,  $X_{cd,m}$  and corresponding  $x_{cd}$  in situ measurements. Results obtained using 2 GHz and 5 V e-APD bias voltage.

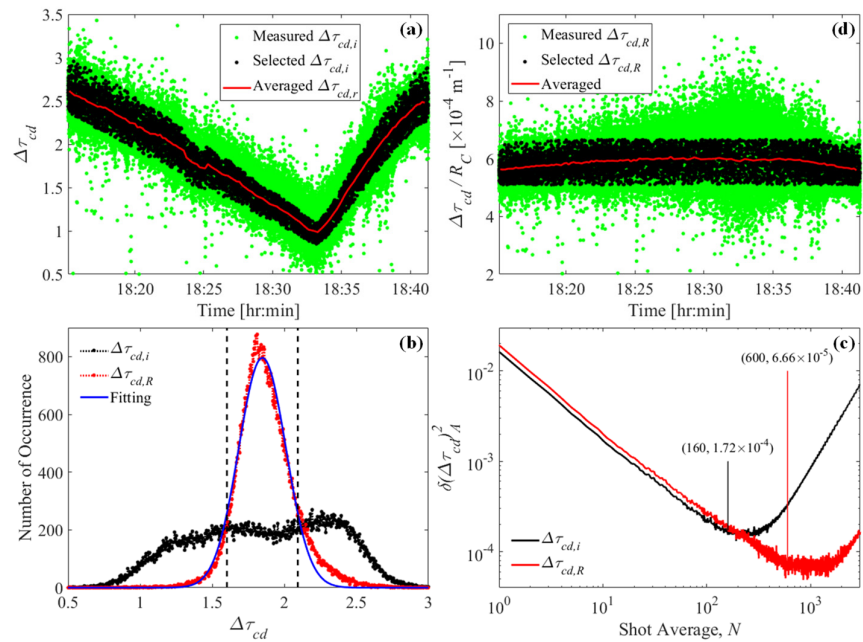


**Figure 17.** Summary of the airborne pulsed 2- $\mu\text{m}$  IPDA lidar statistical analysis of  $\Delta\tau_{cd}$  measurement. (a) Single-shot IPDA  $\Delta\tau_{cd,i}$  measurements, selected shots and 500 shot average. (b) Statistical distribution of  $\Delta\tau_{cd,i}$  and range-normalized  $\Delta\tau_{cd,R}$  with normal distribution fitting. Vertical dashed lines mark  $\pm 1.5$  standard deviation for the fitting. (c) Allan-variance analysis for  $\Delta\tau_{cd,i}$  and range-normalized  $\Delta\tau_{cd,R}$ . (d) range-normalized single-shot  $\Delta\tau_{cd,R}$ , selected shots and 500 shot average.

Figure 18 shows similar analysis for Spiral 2 record conducted after sunset. Reproduction of similar results indicates consistent performance of the IPDA lidar. Using IPDA measurement, the retrieved  $X_{cd}$  variation with altitude is shown in Figure 19 after additional 200-m range-bin average. Range-bin average enhances  $X_{CO_2}$  retrievals, resulting in vertical  $X_{cd}$  profiles with enhanced precision and resolution, as listed in Table 2. Higher  $X_{cd}$  variability with altitude is observed for Spiral 2, after sunset, as compared to Spiral 1, before sunset. This is attributed to higher winds occurring after sunset due to land breeze, which is a common phenomenon for coastal regions.

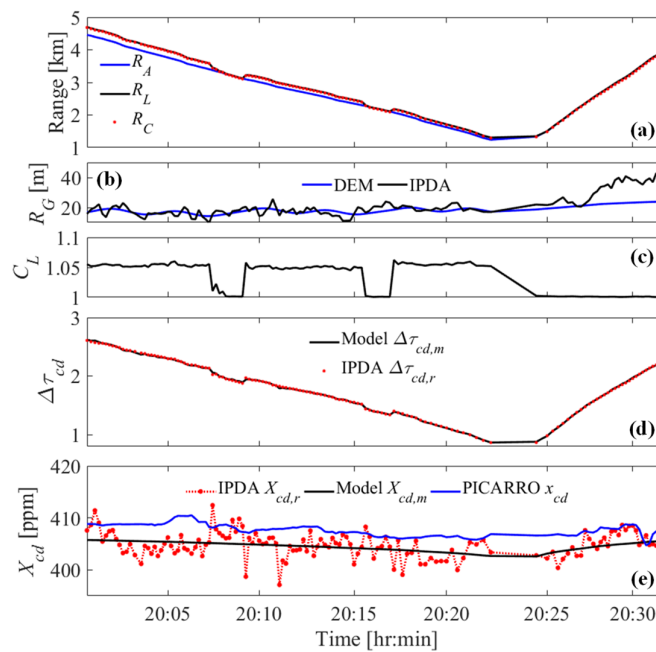


**Figure 18.** Airborne pulsed 2- $\mu$ m IPDA lidar measurement and retrieval results during Spiral 2 conducted after sunset. (a) Airborne altitude,  $R_A$ , as compared to LOS,  $R_L$  and IPDA column measurement,  $R_C$ . (b) Estimated ground elevation,  $R_G$ , as compared to DEM results. (c) Corresponding  $C_L$  profile used for converting  $R_A$  to  $R_L$ . (d) IPDA  $\Delta\tau_{cd}$  measurement after processing and 10-s (500 shots) average,  $\Delta\tau_{cd,r}$  compared to model  $\Delta\tau_{cd}$ ,  $\Delta\tau_{cd,m}$ , obtained from MGD. (e) IPDA retrieved  $X_{CO_2}$ ,  $X_{cd,r}$ , compared to model driven  $X_{CO_2}$ ,  $X_{cd,m}$  and corresponding  $x_{cd}$  in situ measurements. Results obtained using 2 GHz and 5.5 V e-APD bias voltage.

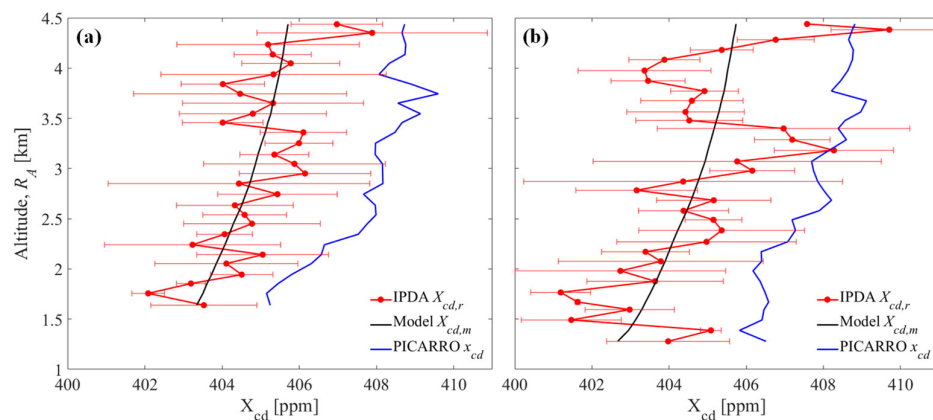


**Figure 19.** Airborne pulsed 2- $\mu$ m IPDA lidar  $X_{cd,r}$  retrieval enhanced using 200-m range-bin average for (a) Spiral 1 before sunset and (b) Spiral 2 after sunset. Horizontal bars indicated retrieval standard deviation within each range-bin. Results are compared to MGD model,  $X_{cd,m}$ , and in situ measurements  $x_{cd}$ .

### 4.3. Clouds Record

To capture free-tropospheric  $X_{CO_2}$ , the IPDA lidar was operated while flying over the thick cloud cover using the top of the clouds as target. Using cloud target, IPDA measurement results are shown in Figure 20, representing the third section of Figure 12. Cloud height, shown in Figure 20), was calculated as target elevation using IPDA column length, shown in Figure 20b, GPS altitude and INS attitude. Figure 20c indicates maximum and minimum detected powers of 3.79 and 0.23  $\mu W$ , respectively, for both on- and off-line pulses throughout that record, as marked in Figure 4. IPDA measured  $\Delta\tau_{cd}$  is obtained using Equation (5) and compared to the corresponding updated model value in Figure 20d after 50 shot average. Statistical analysis indicates a mean and standard deviation of  $0.7921 \pm 0.1961$  and  $0.7432 \pm 0.2032$  for IPDA measured and modeled  $\Delta\tau_{cd}$  results, respectively. Measured  $\Delta\tau_{cd}$  was converted to  $X_{cd}$ , using Equation (13), and compared to model in Figure 20e. Statistical results of  $X_{cd}$  measurement is presented in Table 2. Although high correlation ( $> 95\%$ ) was observed between measured  $\Delta\tau_{cd}$  and associated model, with 97.3% success rate,  $X_{cd}$  retrieval exhibited limited sensitivity. The observed sensitivity through these challenging conditions, is attributed to the nature of cloud targets. High range variability within the laser footprint on a cloud target, as indicated by irregular return pulse profiles of Figure 12c,d for example, affects shot averaging and determination of pulse integration limits, which directly contributes to return power precision and  $\Delta\tau_{cd}$  random and systematic errors. In addition, high  $H_2O$  content within cloud layers results in higher molecular interference and higher uncertainties in  $N_{dry}$  determination that directly contributes to  $\Delta\tau_{cd}$  systematic error.

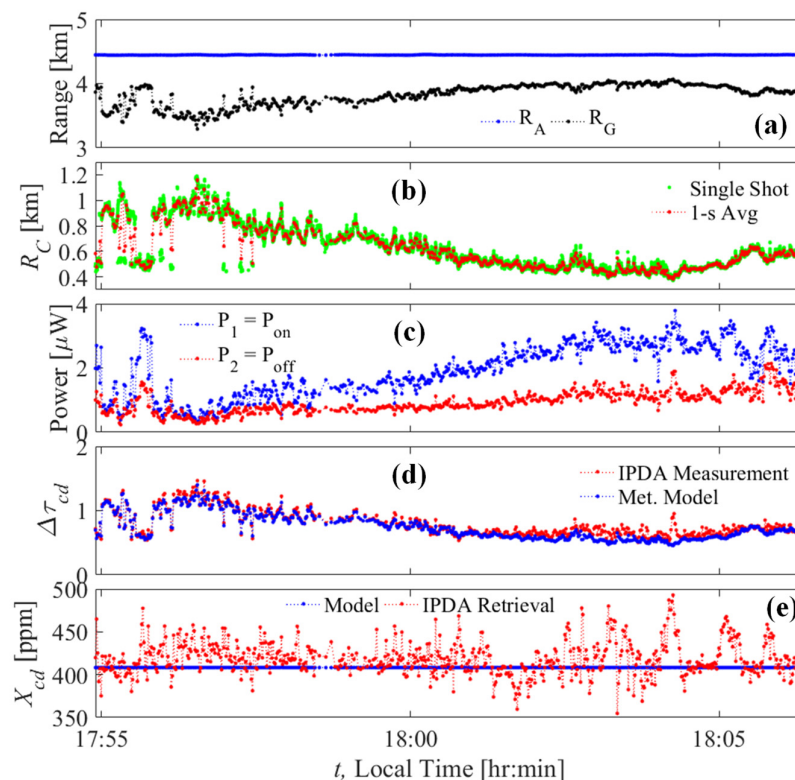


**Figure 20.** Airborne pulsed 2- $\mu m$  IPDA lidar measurement results using nadir thick clouds target. (a) GPS altitude and estimated target elevation, obtained using (b) IPDA column length measurements. Shot average of 1-s (50 shots) was applied to (c) on- and off-line return powers, set to pulse 1 and 2, respectively. (d) IPDA measured  $CO_2$  differential optical depth as compared to modeled  $CO_2$  differential optical depth derived using MGD of Figure 8. (e) Retrieved  $X_{cd}$ , using IPDA measurement, as compared to model. Results are obtained using e-APD detection channel set to 3 V bias and 0.5 GHz on-line wavelength.

## 5. Conclusions

Airborne 2- $\mu\text{m}$  IPDA lidar capability for high-accuracy and high-precision active remote sensing of weighted-average column dry-air volume mixing of  $\text{CO}_2$  was demonstrated. The IPDA lidar, developed at NASA LaRC, is an upgrade from the triple-pulse instrument for double-pulse operation focusing only on  $\text{CO}_2$  Measurements. The upgrade included stable laser transmitter performance with enhanced monitoring for pulse properties and using an advanced MCT e-APD detection system. Other support instruments are used for updating IPDA lidar prediction models and  $\text{XCO}_2$  retrieval during airborne operation. The instrument targets the R30  $\text{CO}_2$  absorption line, which characterized by lower temperature sensitivity and optimum absorption in the lower troposphere. Therefore, MSL atmospheric model presents close temperature and pressure estimates to profiles obtained from support instruments, during experiment time. Updated IPDA instrument model included range correction factor arise due airborne platform attitude, by which sensing column length deviates from perfect vertical nadir during sharp aircraft maneuvers such as spirals. Error budget, for  $X_{\text{cd}}$  retrieval, predicts lower random error for longer sensing column length, indicating preference for higher altitude operation. Further enhanced random error is attained using on-line closer to R30 line center. Systematic error is dominated by water vapor through dry-air number derivation, followed by water vapor interference and ranging related errors.

This study focuses on four hours validation flight, during tropical storm Imelda, which covers five distinct IPDA data records under diverse environmental conditions. These conditions included fixed altitude over ocean and spiral descend over land targets in clear-sky before and after sunset, as well as targeting thick-cloud cover to capture free-tropospheric  $\text{XCO}_2$ . The IPDA lidar performed well during these conditions. Oceanic surface target is characterized by low but consistent surface reflectivity providing steady elevation in moderate-state, which is suitable for minimizing range uncertainties. IPDA results using ocean surface indicated  $404.43 \pm 1.23$  ppm IPDA  $\text{XCO}_2$  measurement with 0.26% and 0.30% relative accuracy and precision, respectively as compared to instrument model prediction of  $405.49 \pm 0.01$  ppm. Gradual airborne spiral descend provided an opportunity for updating meteorological data variation with altitude and the capability for range-bin average for enhanced  $\text{XCO}_2$  retrievals. IPDA spiral results in  $404.89 \pm 1.19$  as compared to model derived  $404.75 \pm 0.73$  indicating 0.04% and 0.23% relative accuracy and precision, respectively. Although better than 95% correlation between IPDA and model results was observed for cloud targets, limited accuracy and precision were observed. Clouds targets are challenging in terms of water vapor and ranging uncertainties, which are the dominant systematic error sources. Ranging contributes to random error due to higher variability within the laser footprint over clouds. In addition, high water vapor content within cloud layers results in higher molecular interference and higher ambiguities in dry-air number density determination, directly contributing systematic errors. This IPDA lidar demonstrated reliability, operational readiness, and improved performance.

**Author Contributions:** Conceptualization, T.F.R., M.P. and U.N.S.; methodology, T.F.R. and M.P.; software, C.W.A.; formal analysis, T.F.R.; investigation, T.F.R., M.P., C.W.A., Y.C., J.V.P. and J.P.D.; resources, C.W.A., Y.C., J.V.P., J.P.D. and A.N.; writing—original draft preparation, T.F.R.; writing—review and editing, T.F.R., M.P. and J.D; supervision, U.N.S.; project administration, M.P. and A.N.; funding acquisition, U.N.S. All authors have read and agreed to the published version of the manuscript.

**Funding:** This research received no external funding.

**Conflicts of Interest:** The authors declare no conflict of interest.

## References

- National Academies of Sciences, Engineering, and Medicine. *Thriving on Our Changing Planet: A Decadal Strategy for Earth Observation from Space*; The National Academies Press: Washington, DC, USA, 2018.
- Wunch, D.; Toon, G.; Blavier, J.; Washenfelder, R.; Notholt, J.; Connor, B.; Griffith, D.; Sherlock, V.; Wennberg, P. The total carbon column observing network. *Philos. Trans. R. Soc. A* **2011**, *369*, 2087–2112.
- Sweeney, C.; Karion, A.; Wolter, S.; Newberger, T.; Guenther, D.; Higgs, J.; Andrews, A.; Lang, P.; Neff, D.; Dlugokencky, E.; et al. Seasonal climatology of CO<sub>2</sub> across North America from aircraft measurements in the NOAA/ESRL global greenhouse gas reference network. *J. Geophys. Res.* **2015**, *120*, 5155–5190.
- Wunch, D.; Wennberg, P.O.; Osterman, G.; Fisher, B.; Naylor, B.; Roehl, C.M.; O'Dell, C.; Mandrake, L.; Viatte, C.; Kiel, M.; et al. Comparisons of the Orbiting Carbon Observatory-2 (OCO-2) X<sub>CO2</sub> measurements with TCCON. *Atmos. Meas. Tech.* **2017**, *10*, 2209–2238.
- Eldering, A.; Taylor, T.; O'Dell, C.; Pavlick, R. The OCO-3 mission: Measurement objectives and expected performance based on 1 year of simulated data. *Atmos. Meas. Technol.* **2019**, *12*, 2341–2370.
- Singh, U.; Refaat, T.; Ismail, S.; Davis, K.; Kawa, S.; Menzies, R.; Petros, M. Feasibility study of a space-based high pulse energy 2 μm CO<sub>2</sub> IPDA lidar. *Appl. Opt.* **2017**, *56*, 6531–6547.
- Kawa, S.; Abshire, J.; Baker, D.; Browell, E.; Crisp, D.; Crowell, S.; Hyon, J.; Jacob, J.; Jucks, K.; Lin, B.; Menzies, R.; et al. Active sensing of CO<sub>2</sub> emissions over nights, days, and seasons (ASCENDS): Final Report of the ASCENDS Ad Hoc Science Definition Team. *NASA/TP* **2018**, 219034.
- Refaat, T.; Petros, M.; Singh, U.; Antill, C.; Remus, R. High-precision and high accuracy column dry-air mixing ratio measurement of carbon dioxide using pulsed 2-μm IPDA lidar. *IEEE Trans. Geosci. Remote Sens.* **2020**, *58*, 5804–5819.
- National Research Council. *National Imperatives for the Next Decade and Beyond Committee on Earth Science and Applications from Space: A Community Assessment and Strategy for the Future*; National Academies: Washington, DC, USA, 2007.
- Singh, U.; Walsh, B.; Yu, J.; Petros, M.; Kavaya, M.; Refaat, T.; Barnes, N. Twenty years of Tm:Ho:YLF and LuLiF laser development for global wind and carbon dioxide active remote sensing. *Opt. Mater. Express* **2015**, *5*, 827–837.
- Refaat, T.; Ismail, S.; Koch, G.; Rubio, M.; Mack, T.; Notari, A.; Collins, J.; Lewis, J.; De Young, R.; Choi, Y.; et al. Backscatter 2-μm lidar validation for atmospheric CO<sub>2</sub> differential absorption lidar applications. *Trans. Geosci. Remote Sens.* **2011**, *49*, 572–580.
- Refaat, T.; Ismail, S.; Abedin, N.; Spuler, S.; Mayor, S.; Singh, U. Lidar backscatter signal recovery from phototransistor systematic effect by deconvolution. *Appl. Opt.* **2008**, *47*, 5281–5295.
- Refaat, T.; Ismail, S.; Koch, G.; Diaz, L.; Davis, K.; Rubio, M.; Abedin, N.; Singh, U. Field-testing of a two-micron DIAL system for profiling atmospheric carbon dioxide. In *Proceeding of the 25th International Laser Radar Conference*, St. Petersburg, Russia, 5–9 July 2010; pp. 866–869.
- Yu, J.; Petros, M.; Singh, U.; Refaat, T.; Reithmaier, K.; Remus, R.; Johnson, W. An airborne 2-μm double-pulsed direct-detection lidar instrument for atmospheric CO<sub>2</sub> column measurements. *J. Atmos. Ocean. Technol.* **2017**, *34*, 385–400.
- Refaat, T.; Singh, U.; Petros, M.; Remus, R.; Yu, J. Self-calibration and laser energy monitor validations for a double-pulsed 2-μm CO<sub>2</sub> integrated path differential absorption lidar application. *Appl. Opt.* **2015**, *54*, 7240–7251.
- Refaat, T.; Singh, U.; Yu, J.; Petros, M.; Remus, R.; Ismail, S. Double-pulse 2-μm integrated path differential absorption lidar airborne validation for atmospheric carbon dioxide measurement. *Appl. Opt.* **2016**, *55*, 4232–4246.
- Refaat, T.; Singh, U.; Yu, J.; Petros, M.; Remus, R.; Ismail, S. Airborne two-micron double-pulse IPDA lidar validation for carbon dioxide measurements over land. In *Proceeding of the 28th International Laser Radar Conference*, Bucharest, Romania, 25–30 June 2017; p. 5001.
- Refaat, T.; Singh, U.; Yu, J.; Petros, M.; Ismail, S.; Kavaya, M.; Davis, K. Evaluation of an airborne triple-pulsed 2 μm IPDA lidar for simultaneous and independent atmospheric water vapor and carbon dioxide measurements. *Appl. Opt.* **2015**, *54*, 1387–1398.
- Petros, M.; Singh, U.; Yu, J.; Refaat, T. Development of double-pulsed two-micron laser for atmospheric carbon dioxide measurements. In *Proceedings of the Conference on Lasers and Electro-Optics*, San Jose, CA, USA, 14–19 May 2017; JTh2A.8.
- Petros, M.; Refaat, T.; Singh, U.; Antill, C.; Remus, R.; Wong, T.; Lee, J.; Ismail, S. Frequency control of multi-pulse 2-micron laser transmitter for atmospheric carbon dioxide measurement. In *Proceedings of the IGARSS 2019 IEEE International Geoscience and Remote Sensing Symposium*, Piscataway, NJ, USA, 28 July–2 August 2019; pp. 4857–4860.
- Refaat, T.; Petros, M.; Singh, U.; Antill, C.; Wong, T.; Remus, R.; Reithmaier, K.; Lee, J.; Bowen, S.; Taylor, B.; et al. Airborne, direct-detection, 2-μm triple-pulse IPDA lidar for simultaneous and independent atmospheric water vapor and carbon dioxide active remote sensing. *Proc. SPIE* **2018**, *10779*, 1077902.
- Refaat, T.; Petros, M.; Remus, R.; Singh, U. MCT APD detection system for atmospheric profiling applications using two-micron lidar. *EPJ Web Conf.* **2020**, *237*, 01013.
- Bagheri, M.; Spiers, G.; Frez, C.; Forouhar, S. Line width Measurement of distributed-feedback semiconductor Lasers operating near 2.05-μm. *IEEE Photon. Technol. Lett.* **2015**, *27*, 1934–1937.
- Gordon, I.E.; Rothman, L.S.; Hill, C.; Kochanov, R.V.; Tan, Y.; Bernath, P.F.; Birk, M.; Boudon, V.; Campargue, A.; Chance, K.V.; et al. The HITRAN2016 molecular spectroscopic database. *J. Quant. Spectrosc. Radiat. Transf.* **2017**, *203*, 3–69.
- Rothman, L.S.; Rinsland, C.P.; Goldman, A.; Massie, S.T.; Edwards, D.P.; Flaud, J.M.; Perrin, A.; Camy-Peyret, C.; Dana, V.; Mandin, J.Y.; et al. The HITRAN molecular spectroscopic database and HAWAKS (HITRAN atmospheric workstation): 1996 edition. *J. Quant. Spectrosc. Radiat. Transf.* **1998**, *60*, 665–710.

26. Refaat, T.; Petros, M.; Lee, J.; Wong, T.; Remus, R.; Singh, U. Laser energy monitor for triple-pulse 2- $\mu\text{m}$  IPDA lidar application. *Proc. SPIE* **2018**, 10779, 1077905.
27. Menzies, R. Coherent and incoherent Lidar—An overview. In *Tunable Solid State Lasers for Remote Sensing*; Springer: Berlin, Germany, 1985; pp. 17–21.
28. Casse, V.; Gibert, F.; Edouart, D.; Chomette, O.; Crevoisier, C. Optical energy variability induced by speckle: The cases of MERLIN and CHARM-F IPDA lidar. *Atmosphere* **2019**, 10, 540.
29. Sun, X.; Abshire, J.; Krainak, M.; Lu, W.; Beck, J.; Sullivan, W.; Mitra, P.; Rawlings, D.; Fields, R.; Hinkley, D.; et al. HgCdTe avalanche photodiode array detectors with single photon sensitivity and integrated detector cooler assemblies for space lidar applications. *Opt. Eng.* **2019**, 58, 067103.
30. Sun, X.; Abshire, J.; Beck, J.; Mitra, P.; Reiff, K.; Yang, G. HgCdTe avalanche photodiode detectors for airborne and space borne lidar at infrared wavelengths. *Opt. Exp.* **2017**, 25, 16589–16602.
31. Refaat, T.; Singh, U.; Petros, M.; Remus, R. MCT avalanche photodiode detector for two-micron active remote sensing applications. In *Proceeding of the IEEE International Geoscience and Remote Sensing Symposium, Valencia, Spain, 22–27 July 2018*; pp. 1865–1868.
32. Anderson, G.; Clough, S.; Kneizys, F.; Chetwynd, J.; Shettle, E. AFGL atmospheric constituent profiles (0–120 km). In *Environmental Research Papers*; AFGL-TR-86-0110 No. 954; Air Force Geophysics Laboratory: Hanscom AFB, MA, USA, 1986.
33. Ehret, G.; Kiemle, C.; Wirth, M.; Amediek, A.; Fix, A.; Houweling, S. Space-borne remote sensing of CO<sub>2</sub>, CH<sub>4</sub> and N<sub>2</sub>O by integrated path differential absorption Lidar: A sensitivity analysis. *Appl. Phys. B* **2008**, 90, 593–608.